Sensors & Actuators: B. Chemical 417 (2024) 136170

Contents lists available at ScienceDirect

Sensors and Actuators: B. Chemical

journal homepage: www.elsevier.com/locate/snb

NO_2 gas-sensing enhancement by selective laser surface treatment of SnO_2 nanorods

Changhyun Jin [a,b,1], Hyunseong Yang [a,1], Taewon Lim [a], Kyu Hyoung Lee [a,*], Wooyoung Lee [a,*]

[a] Department of Materials Science and Engineering, Yonsei University, Seoul 03722, the Republic of Korea
[b] KIURI Institute, Yonsei University, Seoul 03722, the Republic of Korea

ARTICLE INFO

Keywords:
SnO2
Nanostructure
Laser
Gas sensor

ABSTRACT

A new surface engineering technology has been introduced that can dramatically change the morphology and composition of existing SnO_2 nanorods (NRs) to SnO_x nanobeads (NBs) + NRs with the addition of a 1–6s laser + convex lens pair (LCP) process. Unlike the existing flame chemical vapour deposition (FCVD) method, which has a two-dimensional effect on a sample, LCP can control a relatively local area with a radius of several microns, making it a more sophisticated and advanced process. Notably, the LCP process at each second was directly linked to the change in the composition of the surface of the SnO_2 NRs, and the response to NO_2 gas in the SnO_2 NBs + NRs with 1second LCP process was improved by approximately three times compared to that of bare SnO_2 NRs. Therefore, a new gas-sensing mechanism was proposed through comparing the types of oxygen defect on the SnO_2 NRs surface during a slight morphological transition and thermodynamic data of the composition before and after gas sensing.

1. Introduction

Thus far, in gas sensing, the probability (frequency) of physical/chemical adsorption between the target gas and the surface can be increased significantly in the following four categories:

First, there may be a method to increase the cross-sectional area (CSA) where the target gas and surface meet [1,2]. For example, if the surface is created at a positive angle with respect to the substrate (that is, higher than the surface of the substrate), the response area corresponding to the area of the circle increases further. However, even if the surface is created at a negative angle with respect to the substrate (that is, lower than the surface of the substrate), the depth of the substrate inevitably increases. For example, An et. al. [3] changed bare SnO2 to 1.5 % In2O3 doped SnO2 by doping In2O3 into SnO2 using coprecipitation and increased the Brunauer–Emmett–Teller (BET) surface area from 23.5 cm2/g to 43.8 cm2/g. Therefore, it exhibited a high response of up to 76.5 at 140 °C for 50 ppm n-butanol sensing. Park et. al. [4] showed that the porosity and nanotubular structure formed by the Kirkendall effect [5] in the SnO2-CuO nanocomposites structure provide a wider surface area than the nanofibre structure, resulting in a high response of 1395–5 ppm H2S gas at 200 °C.

Second, there is a method for forming defects of different dimensions so that the target gas can be well-adsorbed on the surface of the semiconductor [6,7]. That is, as the 0-dimensional kink develops from the 2-dimensional terrace through the 1-dimensional ledge, the physical/chemical adsorption point with the target gas increases, so that the number of mobile carriers can also increase. We have previously reported that the same type of target gas can exhibit different responses depending on which part of the target gas is adsorbed on the terrace, ledge, or kink [8,9]. That is, through detection of ethanol gas, n-typed WO3 [8] and p-typed TeO2 [9] nanostructures were confirmed. Han et. al. [10] also reported that octahedral SnO2 exhibits different chemical activities not only on different sides but also on TLK through ethanol gas sensing at different concentrations.

Third, assuming that the process temperature is the same, the crystallinity can be adjusted to affect the concentration and mobility of mobile carriers in the conduction channel formed on the substrate [11,12]. That is, even under the same conditions, the concentration and mobility of mobile carriers can be greatly affected depending on whether they are amorphous, single-crystal, or polycrystalline, which eventually plays an important role in the performance of gas sensing. In general, amorphous materials do not guarantee stability (consistency) in

* Corresponding authors.
E-mail addresses: khlee2018@yonsei.ac.kr (K.H. Lee), wooyoung@yonsei.ac.kr (W. Lee).
[1] Changhyun Jin and Hyunseong Yang had equal contribution as co-first authors.

https://doi.org/10.1016/j.snb.2024.136170
Received 5 September 2023; Received in revised form 18 June 2024; Accepted 20 June 2024
Available online 24 June 2024

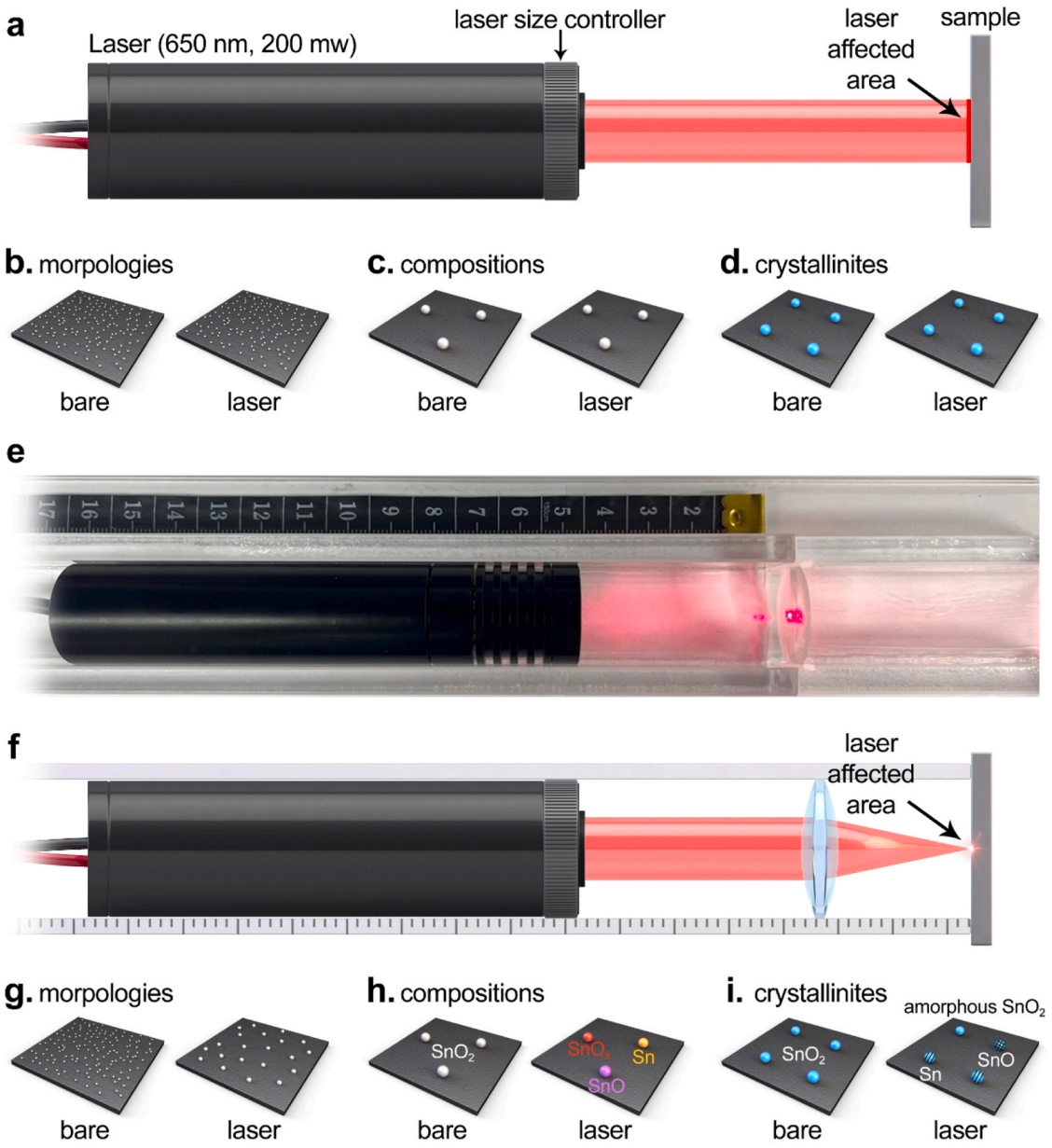

Fig. 1. Schematic diagram comparing the effects of laser and LCP. (a) laser specifications and (b–d) Conceptual diagram of laser energy that does not affect (b) morphology, (c) composition and (d) crystallinity. (e) Image of real LCP. (f–i) Conceptual diagram of (f) LCP and laser energy that affects (g) morphology, (h) composition and (i) crystallinity.

gas sensing, especially at high temperatures. Thus, a single crystalline material can provide stability with respect to grain size. However, polycrystalline materials are generally used owing to the relatively high cost and technical limitations of monocrystalline materials, given their advantages in terms of structural stability, small grain size, large area, inexpensive design technology, and good electrophysical properties [13, 14].

Fourth, there may be a method for increasing the surface energy state of the matrix [15,16]. Compositionally, many types of unstable bonds can form in nonequilibrium states. This, in turn, may be the main cause of the increase in the probability of adsorption of oxygen ion species present at different temperatures before the adsorption of the target gas and the increase in the number of mobile carriers involved after the adsorption of the target gas. Zhao et. al. [17] reported improved gas detection results for methanol above 70 and formaldehyde above 40, using the synergistic effect of oxygen interstitial and vacancy in Li-doped ZnO nanoparticle films. Al-Hashem et. al. [18] also reported that the initial resistance can be determined by controlling the amount of doping or oxygen in the semiconducting metal oxide heterostructure.

Given these trends, the present work falls into the fourth category mentioned above. Only the relatively flat surfaces of semiconducting SnO2 nanorods (NRs) were selectively changed into slightly bumpy bead surfaces using the laser + convex lens pair (LCP) process for a short time. In other words, in this process, the output of laser concentration, which increases with each second (s), was able to induce different physical and chemical changes on the SnO2 NRs surface. In particular, it has been reported that the response to NO2 gas, which is known to be optimised for n-type semiconductors, is improved by approximately three times with an instantaneous surface change of 1s LCP. This approach is significant in that it is free from existing economic, spatial, and time constraints, and presents the most realistic solution that can achieve the maximum effect with minimum effort. In addition, as a spin-off study during this research process, it is certain that the laser concentration will play a major role in the transition mechanism between n- and p-type

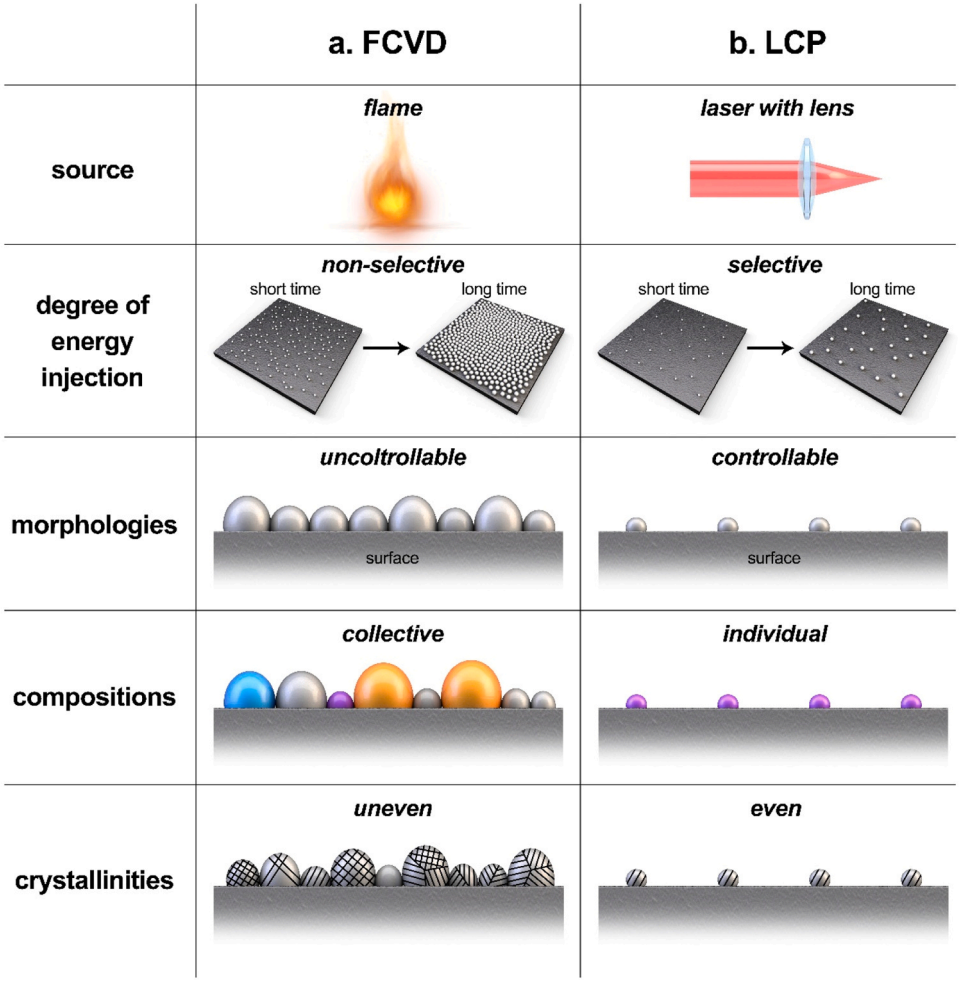

Fig. 2. Comparison of characteristics and effects of the (a) existing FCVD process and (b) proposed LCP process.

semiconductor metal oxide nanostructures, which will be reported subsequently.

2. Experimental section

2.1. Materials

SnO2 NRs were deposited on a 1 × 1 cm Si substrate using glancing angle deposition (GLAD) e-beam equipment. To reduce impurities, residual gas was first removed and GLAD was started in a vacuum state of 2.0 × 10–6 torr or less. The sample was set at an angle of 80° for even deposition. Synthesis was performed for 1 h while giving a rotation of 12 rpm. After this process, the deposited SnO2 NRs with a thickness of 148 nm were annealed at 500 °C for 1 h. The synthesised SnO2 NRs were subjected to laser (650 nm 200 mw) + convex lens (diameter: 23 mm) pair (LCP) treatment for surface modification. The distance between the laser and convex lens was 300 mm, and the distance between the convex lens and SnO2 NRs was fixed at 65 mm. The concentration time of the LCP process on the SnO2 NRs was sequentially increased to 0 s (bare), 1s, 3s, and 6s, and each surface change was observed. At this time, the area affected by the LCP process was within a radius of several microns.

2.2. Characterizations

Field-emission scanning electron microscopy (FE-SEM, JSM-7800 F, JEOL Ltd.), field-emission transmission electron microscopy (FE-TEM, JEM-F200, JEOL Ltd.), energy dispersive X-ray spectroscopy (EDX), and mapping incorporated into TEM were used for morphological and compositional changes on the surface of the SnO2 NRs. X-ray diffraction (XRD; Smart Lab, Rigaku) was performed to determine the crystal phases using Cu-Kα irradiation (λ = 1.5418 Å). Both selected area electron diffraction (SAED) and high-resolution transmission electron microscopy (HRTEM) incorporated into TEM measurements were carried out for crystallographic change. The surface binding, defects, specific surface area, and energy relationships of the SnO2 NRs were measured using X-ray photoelectron spectroscopy (XPS, Thermo Fisher Scientific Co.), porosimeter (BELSORP-MAX G, MicrotracBEL), and ultraviolet photoelectron spectroscopy (UPS, Thermo Fisher Scientific Co.).

2.3. Gas sensing tests

For gas sensing, an Si/SiO2 wafer (oxidation thickness: 300 nm) is used as the substrate, and self-spin coating, photolithography, photoresist (PR) removal, Cr and Pt sputtering, and lift-off patterning are performed sequentially (Supporting Information (SI), Fig. S1a). In this pattern, the SnO2 NRs are synthesised only within a window of 1 mm2 using the GLAD e-beam equipment (SI, Figs. S1b–c). LCP treatment of these SnO2 NRs is performed under different conditions from 1 to 6s. SnO2 NR-based gas sensors were used in the tube furnace measurement, in which the concentrations of reactive and carrier gases were controlled by mass flow controllers (MFCs). At this time, the process temperature and gas flow rate were automatically controlled by a customised LabView software. The concentrations of all target gases were adjusted as a

Table 1
Comparison of process characteristics for various methods.

Our work	Other work						
Advantages	**Materials**	**Equipment**	**Pre- and post-treatment**	**Process temperature**	**Process time**	**Vacuum degree**	**Ref.**
Materials: (SnO_2-basis)	CuO NWs	oxidation reaction	-	600 °C	6 h	air	[27]
	3D-Fe_2O_3 NRs	hydrothermal	annealing	120 °C	120 h	-	[28]
	Graphene-SnO_2 NPs	substrate from chemical solutions (SCS approach)	-	200 °C	10 min	-	[29]
	Pt-NiO thin films	RF sputtering	annealing	-	-	2 mtorr	[30]
	TiO_2 quantum dots	hydrolysis method	-	80 °C	30 min	-	[31]
	Zr-In_2O_3 mesoporous microstructures	nanocasting	sintering	40 °C	24 h	-	[32]
Equipment: (LCP)	ZnO NFs (nanofibers and nanoflowers), NPs	electrospinning hydrothermal solution	sintering	520 °C 150 °C 80 °C	4 h 10 h 24 h	-	[33]
	In_2O_3 hollow NFs	electrospinning	annealing	70 °C	26 h	-	[34]
	Co_3O_4 microrods	electrospinning	calcination	90 °C	4 h	-	[35]
	Pt-loaded SnO_2 microbelts	electrospinning	calcination	90 °C	2 h	-	[36]
	Au-In_2O_3 NTs	thermal evaporation sputtering	TeO_2 template	500 °C	1 h	1.0×10^{-6} Torr	[37]
	MoO_3 NRs	probe ultrasonic	calcination	75 °C	24 h	-	[38]
Pre- and post-treatment: (Nothing)	RuO_2 NRs-Ru NPs	furnace	thermal reduction	340 °C	120 min	$\leq4\times10^{-5}$ Torr	[39]
	TiO_2 NTs-Ag NPs	furnace	anodization	500 °C	2 h	-	[40]
	WO_3 NWs-PtO_x NPs	hydrothermal	sonication	180 °C	48 h	-	[41]
	WO_3 thin films	sol-gel sputtering electrodeposition thermal evaporation atomic layer deposition chemical vapor deposition	annealing	100 °C ~ 500 °C	30 min ~ 2 h	air ~ 2.3×10^{-5} torr	[42]
	GaN NWs-TiO_2 NCs	sputtering	sputtering	650–700 °C	30 sec	-	[43]
	TiO_2 NRs-NiO NPs	furnace	stirring	40 °C 60 °C 600 °C	1 hr (40 °C) 10 min (60 °C) 1 hr (600 °C)	1 torr	[44]
Process temperature: (1300 °C)	ZnO NWs-Pd NPs	furnace	-	400 °C	4 hr	air	[45]
	TiO_2–Er_2O_3 and TiO_2-Ta_2O_5 thin films	sol-gel	annealing	≤150 °C	72 hr	-	[46]
	MgO-WO_3-SnO_2 NCs	sol-precipitation	calcination	60 °C	24 hr	-	[47]
	CeO_2-In_2O_3 NCs	mixing	-	120 °C	3 hr	-	[48]
	Cr_2O_3-ZnO NFs	solution	calcination	60 °C	5 hr	-	[49]
	In_2O_3-ZnO NSs	chemical vapor deposition	-	1000 °C	1 hr	90 torr	[50]
Process time: (Second-basis)	SnO_2 NWs-Cr_2O_3 NCs	furnace	-	620 °C	20 min	$\leq9\times10^{-2}$ torr	[51]
	SnO_2-$SnSe_2$ NCs	self-assembly	-	700 °C	24 min	-	[52]
	α-MoO_3 NSs	pulsed laser deposition	-	600 °C	12 hr	4×10^{-6} mbar	[53]
	In_2O_3-ZnO NWs	solvothermal hydrothermal	annealing	140 °C 60 °C	16 hr 3 hr	-	[54]
	In_2O_3 NPs-GO NSs	Hummers' method co-precipitation	calcination	60 °C	24 hr	-	[55]
	CuO NPs-$Ti_3C_2T_x$ MXene NCs	solvothermal sintering ultrasonication	ball-milling	70 °C	12 hr	-	[56]
Vacuum degree: (Nothing)	SnS_2-TeO_2 NWs	vapor-liquid-solid method atomic layer deposition	annealing	370 °C 150 °C	1 hr	1.4 torr	[57]
	PdO NPs on Si substrate	plasma-enhanced atomic layer deposition	-	80 °C	≥20 min	1 mtorr	[58]
	InO_x doped SnO_2 NCs	RF sputtering plasma-enhanced atomic layer deposition	-	200 °C	≥30 min	5 mtorr	[59]
	SnS_2 flakes	chemical vapor deposition	-	1000 °C	1 hr	air	[60]
	MoS_2 thin films	Plasma-enhanced atomic layer deposition	-	70 °C	≤45 sec	0.18 torr	[61]
	WSe_2 NSs	chemical vapor deposition	-	850 °C	20 min	0.05 torr	[62]

balance between each target gas and dry air. The electrical resistance of the sample was calculated by a nanovoltmeter (Keithley 2182) using a constant current source (Keithley 6220) of 100 nA. The gas-sensing response was expressed as the ratio of the resistance between air (Ra) and the target gas (Rg). The oxidising gas for n-type semiconductors is (Rg-Ra)/Ra, the reducing gas for n-type semiconductors is (Ra-Rg)/Rg, the oxidising gas for p-type semiconductors is (Ra-Rg)/Rg, and the reducing gas for p-type semiconductors is (Rg-Ra)/Ra. In addition, the

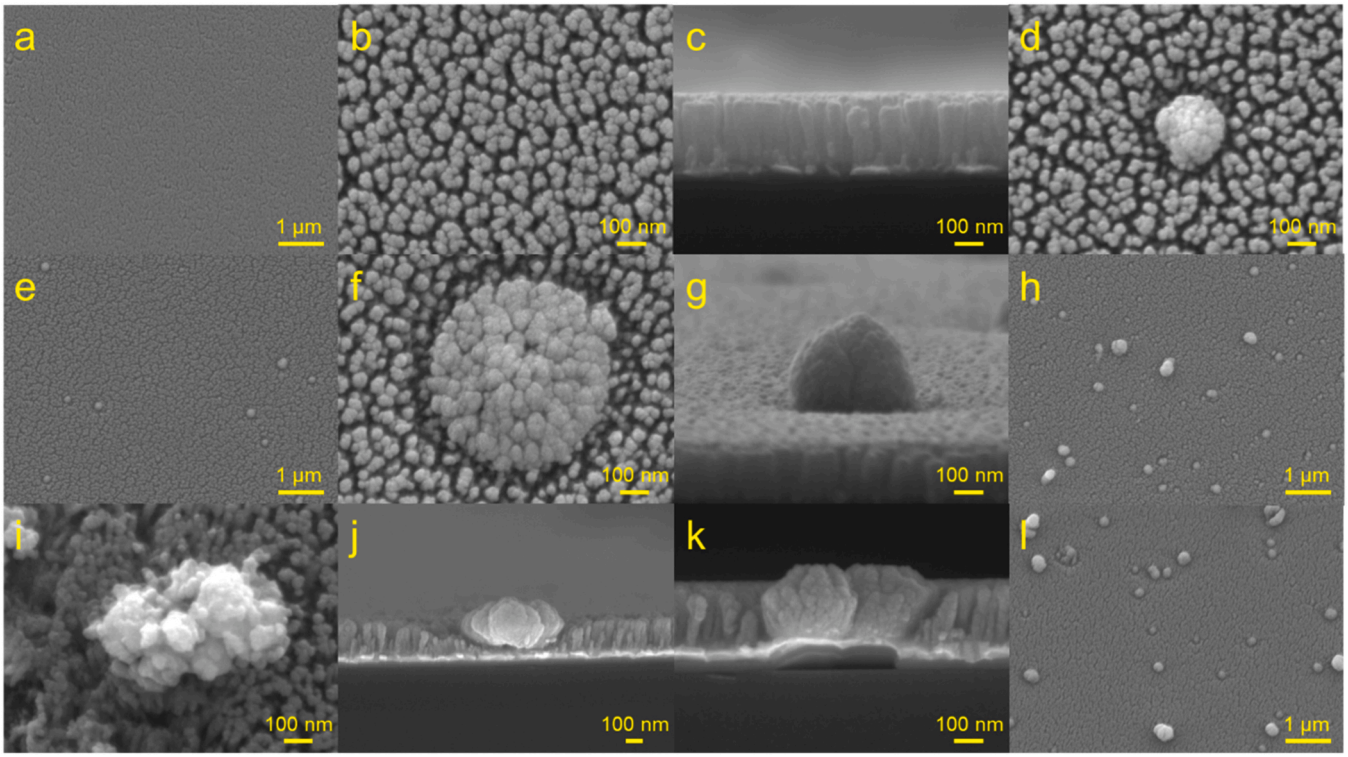

Fig. 3. SEM images showing changes in the morphology of SnO2 NRs applied with 0–6s LCP process. (a-c) Top view and side view SEM images of bare SnO2 NRs. (d, e) SnO2 NBs + NRs SEM image with 1s LCP process. (f–h) SnO2 NBs + NRs SEM image with 3s LCP process. (i–l) SnO2 NBs + NRs SEM image with 6s LCP process. Then, (a), (e), (h), and (l) show SEM images of the same magnification under each condition.

response time (when the target gas was introduced into the air atmosphere) and recovery time (when air was introduced into the target gas atmosphere) were defined based on the point corresponding to 90 % saturation when different gases were present. A specific ratio of relative humidity (RH) of 50 % was obtained using humid air subjected to deionised water bubbling under the same gas-sensing process temperature to compare the sensing response in dry and humid conditions.

3. Results and discussion

To change the morphology, composition, and crystallinity of SnO2 NRs surface within a short time, a laser source capable of adjusting the diameter up to 4.2 mm was used, as shown in Fig. 1a. Although it can affect a large area of the sample, it is believed that SnO2 NRs with a length of approximately 200 nm and a diameter of approximately 50 nm are not sufficiently energetic to cause physicochemical changes (Fig. 1b–d and SI, Fig. S2). However, in the case of an improved LCP process that adds a convex lens to an existing laser (Fig. 1e and f), photons can be gathered at one point and energy can be concentrated. Therefore, as shown in Fig. 1g–i, changes in the physical form, chemical composition, and crystallinity can occur. In particular, this concept makes it possible to mitigate the disadvantage of inevitably influencing the SnO2 NRs sample area, where the influence of the existing laser is not desired over a wide 2-dimensional area (Fig. 2a). That is, depending on the degree of influence of the LCP process, only the desired region can be freely adjusted; for example, (1) morphologically, from a plane to a bead-like particle [19,20]; (2) compositionally, from stoichiometric to non-stoichiometric [21,22]; and crystallographically, from a single crystal (or polycrystalline) to partially amorphous (Fig. 2b) [23,24]. The LCP process is clearly differentiated from the existing flame chemical vapour deposition (FCVD) method [25,26], which is considered to be similar at first glance, as shown in Fig. 2a. That is, the difference in the source as well as the area affecting the sample is clearly distinguished in 2-dimensions. In general, when comparing the SnOx nanobeads (NBs) size, composition ratio, and crystal plane, the FCVD was almost mixed (Fig. 2a), whereas the LCP process could be controlled consistently within a narrow range as a radius of several microns (Fig. 2b).

Table 1 compares the results of previous studies by dividing the superiority of these processes into five categories [27–62]: equipment, pre- and post-treatment, process temperature, process time, and vacuum degree. The advantages of economic, spatial, and time constraints compared with existing processes were reaffirmed.

Fig. 3 shows SEM images of the morphology of SnO2 NRs applied with LCP process from 0 to 6s for use in gas sensing. Fig. 3a-c show top and side views of the SnO2 NRs grown uniformly by GLAD. As shown in the top view, although it consists only of SnO2 NRs without any SnO2 NBs (Fig. 3a), three or four SnO2 NRs tens of nanometres in size gathered at regular intervals and grow as a bundle as a result of the process conditions (Fig. 3b). From the side view, it was confirmed that the SnO2 NRs were tightly aligned (Fig. 3c). When the LCP was applied for 1s, an area was created on the SnO2 NRs, and the SnO2 NRs around the area agglomerated to form approximately 200 nm SnO2 NBs (Fig. 3d). Compared to Fig. 3a for the same area, several SnO2 NBs were formed after only 1s of the LCP process (Fig. 3e). Fig. 3f-h show the changes in the SnO2 NRs during the 3s LCP process. SnO2 NBs grew larger than when a 1s LCP process was applied (Figs. 3f-3g), and it may be observed that SnO2 NBs were formed here and over a wide area owing to the influence of the LCP process (Fig. 3h). Compared to Fig. 3e for the same area, it may be observed that the size and number of SnO2 NBs were more developed in the 3s LCP process (Fig. 3h). However, the condition at the 6s LCP process (Fig. 3i–l) reveals a completely different trend from those mentioned above. The frequency of agglomeration of SnO2 NRs with each other increased; in particular, even the SnO2 NBs were irregular in shape and changed irregularly (Fig. 3i). From the SEM images observed from the side view (Fig. 3j and k), the longer the LCP process time, the shorter the SnO2 NRs and the tendency to agglomerate. Compared to Fig. 3h of the same area, it may be observed that the SnO2 NBs increased in size but collapsed significantly in the 6s LCP process

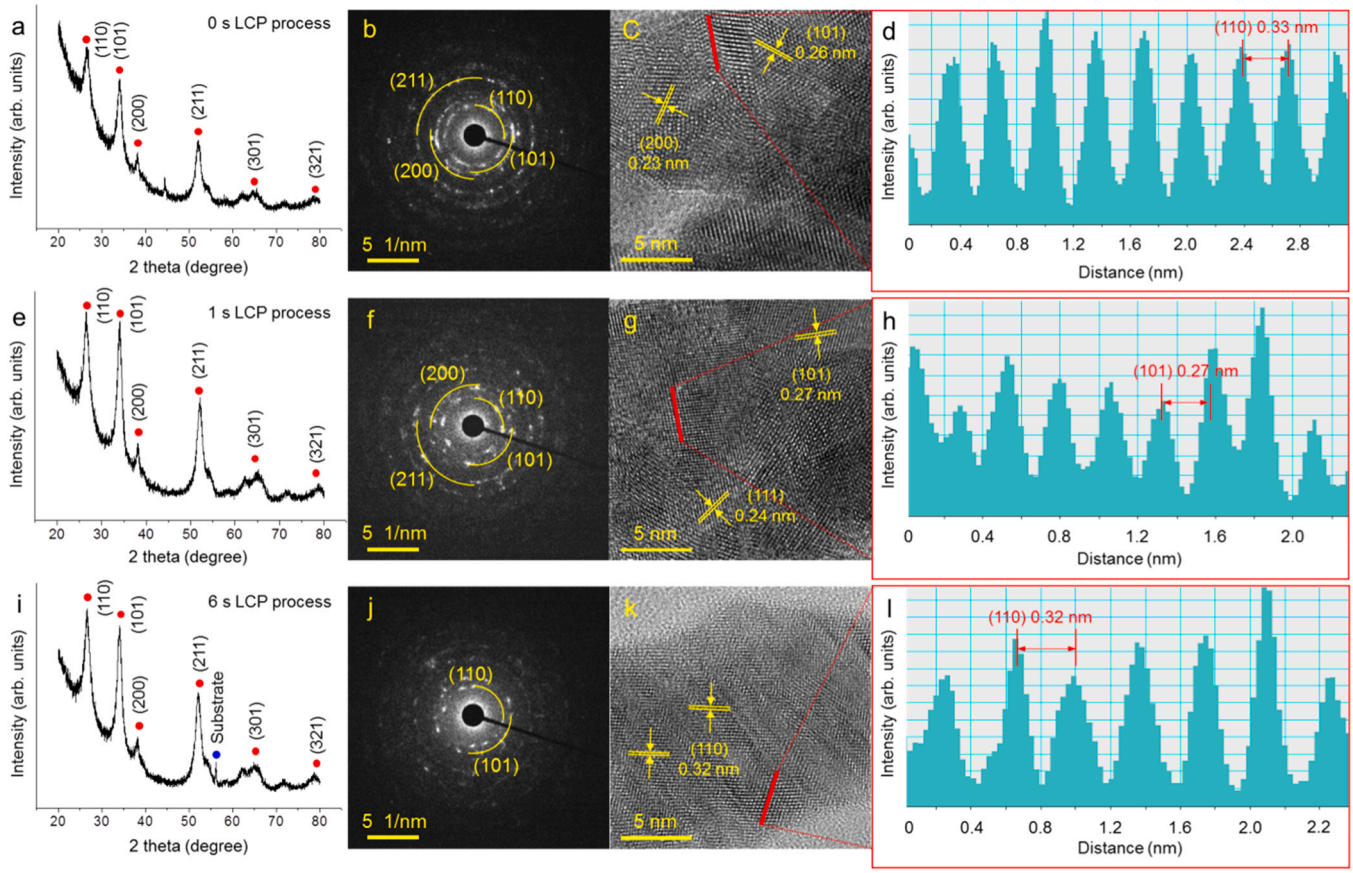

Fig. 4. Crystallinities and microstructures of SnO2 NRs applied with 0, 1, and 6s LCP process. (a–d) Bare SnO2 NRs with 0 s LCP process, (a) XRD, (b) SAED, (c) HRTEM, (d) interplanar spacing. (e–h) SnOx NBs + NRs with l s LCP process, (e) XRD, (f) SAED, (g) HRTEM, (h) interplanar spacing, (i–l) SnOx NBs + NRs with 6s LCP process, (i) XRD, (j) SAED, (k) HRTEM, (l) interplanar spacing.

(Fig. 3l).

From the perspective of gas sensing, the results in Fig. 3 indicate that in the LCP process, especially in a radius of several microns where the laser energy is concentrated, a larger CSA than that of the existing sample may be created.

To examine the effect of the LCP process on the crystallinity of SnO2 NRs, XRD, SAED pattern, HRTEM, and the interplanar spacing of SnO2 NRs with LCP of 0, 1, and 6s were sequentially measured, as shown in Fig. 4. Fig. 4a–d show the bare SnO2 NRs without the LCP process. The XRD peaks in Fig. 4a have (110), (101), (200), (211), (301), and (321) planes for 26.58°, 34.12°, 38.20°, 52.14°, 65.02°, and 78.88°, respectively. This is consistent with tetragonal SnO2 (cell parameters: a = 4.7421, b = 4.7421, and c = 3.1901, JCPDF Card No. 01-077-0449) [63]. The SAED pattern is circular, implying a polycrystalline structure (Fig. 4b) [64,65], and as seen in the HRTEM image, each plane forms a certain regularity in a partial area (Fig. 4c). For example, Fig. 4d indicates an interplanar spacing of approximately 0.33 nm in the (110) plane of the HRTEM image. However, the SnO2 NRs subjected to LCP for 1s were polycrystalline with (101) planes compared with the bare SnO2 NRs (Fig. 4e and f). Examining the interplanar spacing corresponding to HRTEM (Fig. 4g) revealed an interplanar spacing different from that of the SnO2 NRs in some places, which shows that some of the SnO2 NRs can be partially reduced to Sn by the LCP process (Fig. 4h) [66,67]. Fig. 4i–l correspond to the 6s LCP process. At first glance, the XRD pattern was similar to the previous one (Fig. 4i), but some substrate peaks were observed, and the SAED pattern tended to gradually lose polycrystallinity compared with bare SnO2 NRs (Fig. 4j). In addition, HRTEM may deviate slightly from the bare SnO2 NRs in terms of interplanar spacing (Fig. 4k), but there is no drastic change overall (Fig. 4l).

Fig. 5 shows the TEM mapping and point EDX analysis of the three sample types shown in Fig. 4. Overall, Sn and O were uniformly detected under all conditions. However, in the case of bare SnO2 NRs, a trapezoidal shape was also observed, rather than a zigzag shape (Fig. 5a and b). It is believed that the shape can also be controlled according to the GLAD process conditions. The atomic composition was also close to the ratio of the SnO2 NRs (Fig. 5c and d). However, in the case of the 1s LCP process, SnOx NBs can be formed (Fig. 5e and f), and its composition ratio shows that the amount of oxygen is smaller (from 71 at% to 63 at %) and the amount of tin is relatively higher (from 28 at% to 36 at%) compared with bare SnO2 NRs (Fig. 5g and h). In other words, the 1s LCP process not only brings together the existing SnO2 NRs but also shows a tendency of reduction reaction by breaking the binding of the existing Sn-O. However, when the LCP process was increased to 6s, the SnOx NRs agglomerated even if they were not SnOx NBs (Fig. 5i and j). At this time, particularly strong energy was concentrated, and unlike the 1s LCP process, the amount of oxygen increased (from 71 at% to 87 at%) and the amount of tin decreased (from 28 at% to 12 at%) compared with bare SnO2 NRs (Fig. 5k and l). That is, during the 6s LCP process, an increasing amount of O in the surroundings was adsorbed to the sample, showing a tendency toward an oxidation reaction [68,69].

Fig. 6 shows the XPS analysis of the chemical surface binding state of the bare SnO2 NRs, SnOx with the 1s LCP process, and SnOx with the 6s LCP process. First, in the case of the bare SnO2 NRs, it was confirmed that Sn 3d and O 1s were involved (Fig. 6a and b) [70,71]. In this initial situation, when the LCP process is added, it can be seen that, compared with the bare SnO2 NRs, Sn is not very different, but in the case of O, a different peak appears (Fig. 6c and d) [72,73]. That is, based on the 530.68 eV of bare SnO2 NRs, it can be confirmed that the binding energy of 530.08 eV was obtained in the 1s LCP process (Fig. 6c), whereas a

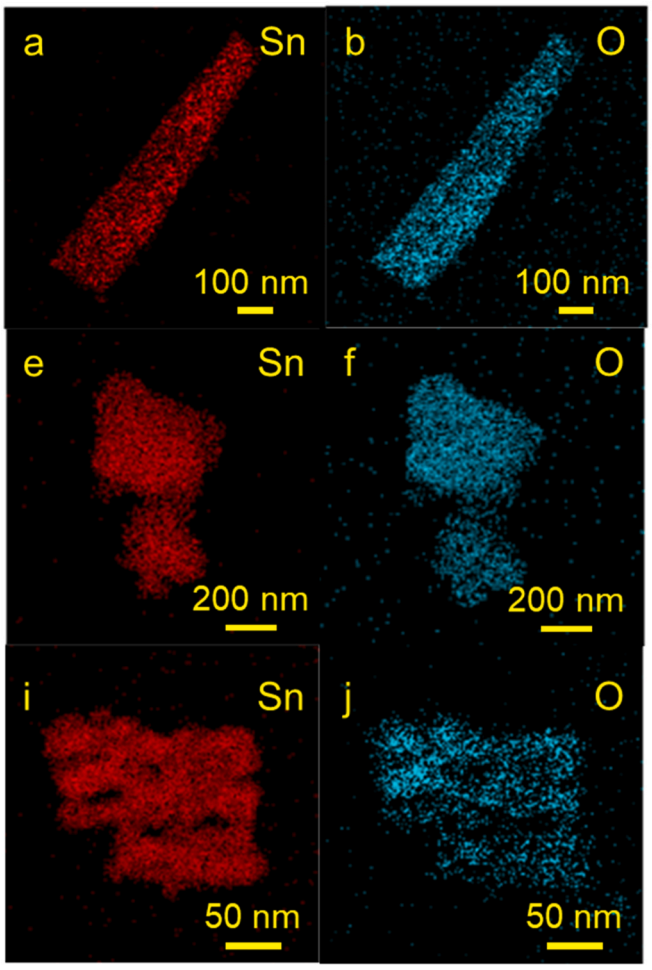

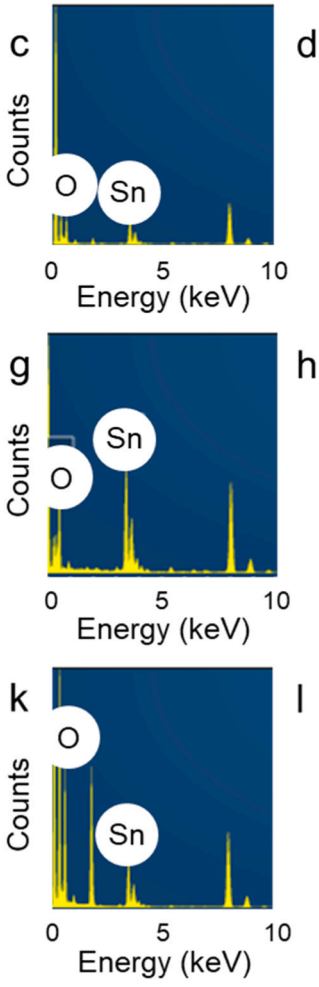

d

Element	Atomic %
Sn	28.38
O	71.62
Total	100.00

h

Element	Atomic %
Sn	36.19
O	63.19
Total	100.00

l

Element	Atomic %
Sn	12.86
O	87.14
Total	100.00

Fig. 5. Changes in composition according to the LCP process. (a, b) Sn and O mapping of bare SnO2 NRs, (a) Sn, (b) O, (c) point EDX of bare SnO2 NRs, (d) at% of bare SnO2 NRs. (e, f) Sn and O mapping of 1s LCP process, (e) Sn, (f) O, (g) point EDX of 1s LCP process, (h) at% of 1s LCP process. (i–l) Sn and O mapping of 6s LCP process, (i) Sn, (j) O, (k) point EDX of 6s LCP process, (l) at% of 6s LCP process.

binding energy of 530.18 eV was also present in the 6s LCP process (Fig. 6d). This implies that non-equilibrium Sn-O bonds were formed on the surface by the LCP process as seen in Fig. 5. Therefore, with the introduction of a simple LCP process, it is possible to engineer a surface that meets the requirements; in particular, it is advantageous that this process is performed within a few seconds.

Gas sensing primarily occurs through a chemical reaction between the target gas and the sample surface, making the state of the sample surface a critical factor in determining the main factors of gas sensing. According to Figs. 7a-7c, in all cases, the content of Sn4+ is higher than that of Sn2+. The difference is the change of the content of Sn2+ or Sn4+ between 0 s and 1s and between 1s and 6s. The deconvoluted Sn 3d XPS spectra of the bare SnO2 NRs are shown in Fig. 7a. The energy of LCP is strong, and thus, in a short time, such as 1s, the energy is used only to cleave the existing bonds between Sn and O. However, heat is generated in the adjacent area after 2 s, and the temperature increases. The surrounding oxygen molecules may accumulate as the temperature increases, and the bonding between Sn and O becomes more active. Therefore, after 2 s, this may be the mechanism of new bond formation of chemisorbed species, including oxidation, which continues. This can be indirectly predicted because more Sn2+ than Sn4+ is present at 1s (Fig. 7b), whereas more Sn4+ than Sn2+ is present at 6s (Fig. 7c). In particular, the type of oxygen formed on the sample surface plays a crucial role in gas sensing. Through deconvolution analysis of XPS in our LCP experiment, we identified the types of oxygen: lattice oxygen (Fig. 7d), oxygen vacancies (Fig. 7e), and chemisorbed oxygen (Fig. 7f). Compared to bare SnO2 NRs, which are dominated by lattice oxygen (Fig. 7d), the 1s LCP conditions led to oxygen vacancies becoming dominant (Fig. 7e), while the 6s LCP conditions favoured chemisorbed oxygen (Fig. 7f). This implies that a reduction reaction of Sn and O occurs during a short LCP process, while an oxidation reaction of Sn and O occurs during a longer LCP process.

However, unlike the change in the composition of SnO2 NRs according to the LCP conditions, the effect on the specific surface area due to the formation of SnO2 NBs was relatively small (SI, Fig. S3). In other words, although the specific surface area may increase depending on the LCP conditions, this increase coincides with the range where the composition changes. Therefore, it can be considered that changing the composition can have a greater impact.

The UPS measurement to investigate the energy relationships, such as the work function and valence band maximum, for each sample are shown in Fig. 8. Both the work function and valence band maximum changed before and after the LCP process (Fig. 8c, f, and i). Specifically, bare SnO2 NRs (Fig. 8a) have a valence band maximum of 3.7 eV (Fig. 8b) and a work function of 4.6 eV by the relationship of 21.2 eV (incident energy) – 16.6 eV (Fig. 8c). Similarly, the sample with 1s LCP process (Fig. 8d) has a valence band maximum of 3.4 eV (Fig. 8e) and a work function of 4.3 eV by the relationship of 21.2 eV (incident energy) – 16.9 eV (Fig. 8 f), and the sample with 6s LCP process (Fig. 8 g) has a valence band maximum of 3.2 eV (Fig. 8 h) and a work function of

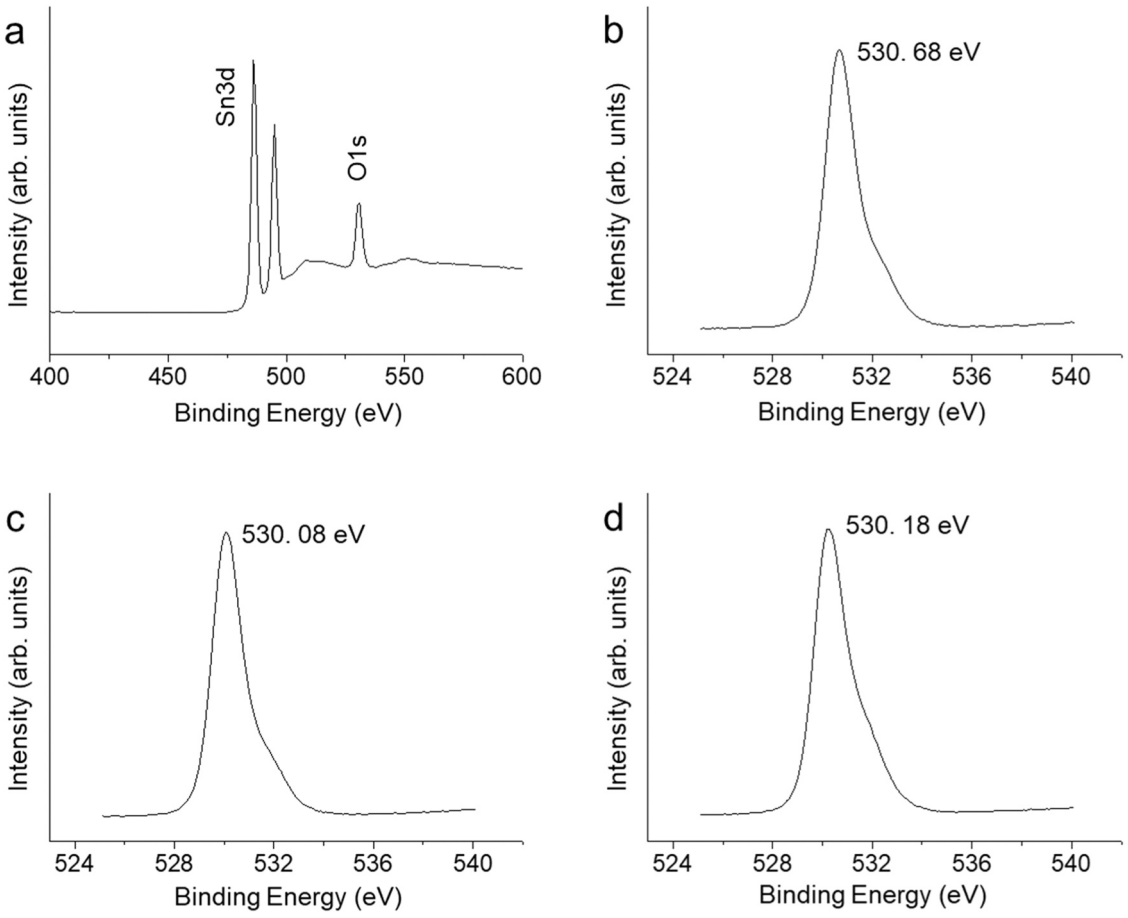

Fig. 6. XPS spectra over LCP process time. (a) Sn 3d and O 1s spectra of bare SnO2 NRs, (b) 530. 68 eV O 1s peak of bare SnO2 NRs, (c) 530. 08 eV O 1s peak of SnOx NBs + NRs with 1s LCP process. (c) 530. 18 eV O 1s peak of SnOx NBs + NRs with 6s LCP process.

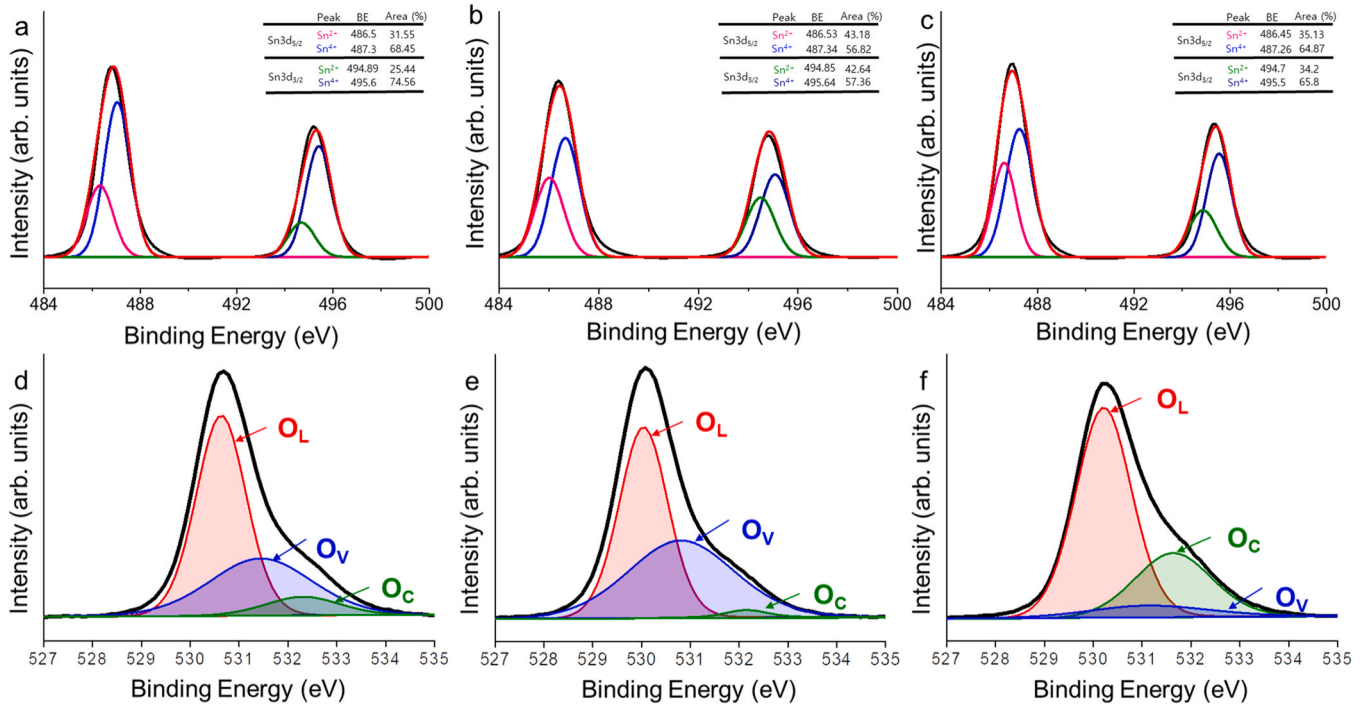

Fig. 7. Deconvoluted (a–c) Sn 3d and (d–f) O 1s XPS spectra of the SnO2 NRs prepared using the (a, d) 0s, (b, e) 1s, or (c, f) 6s LCP process.

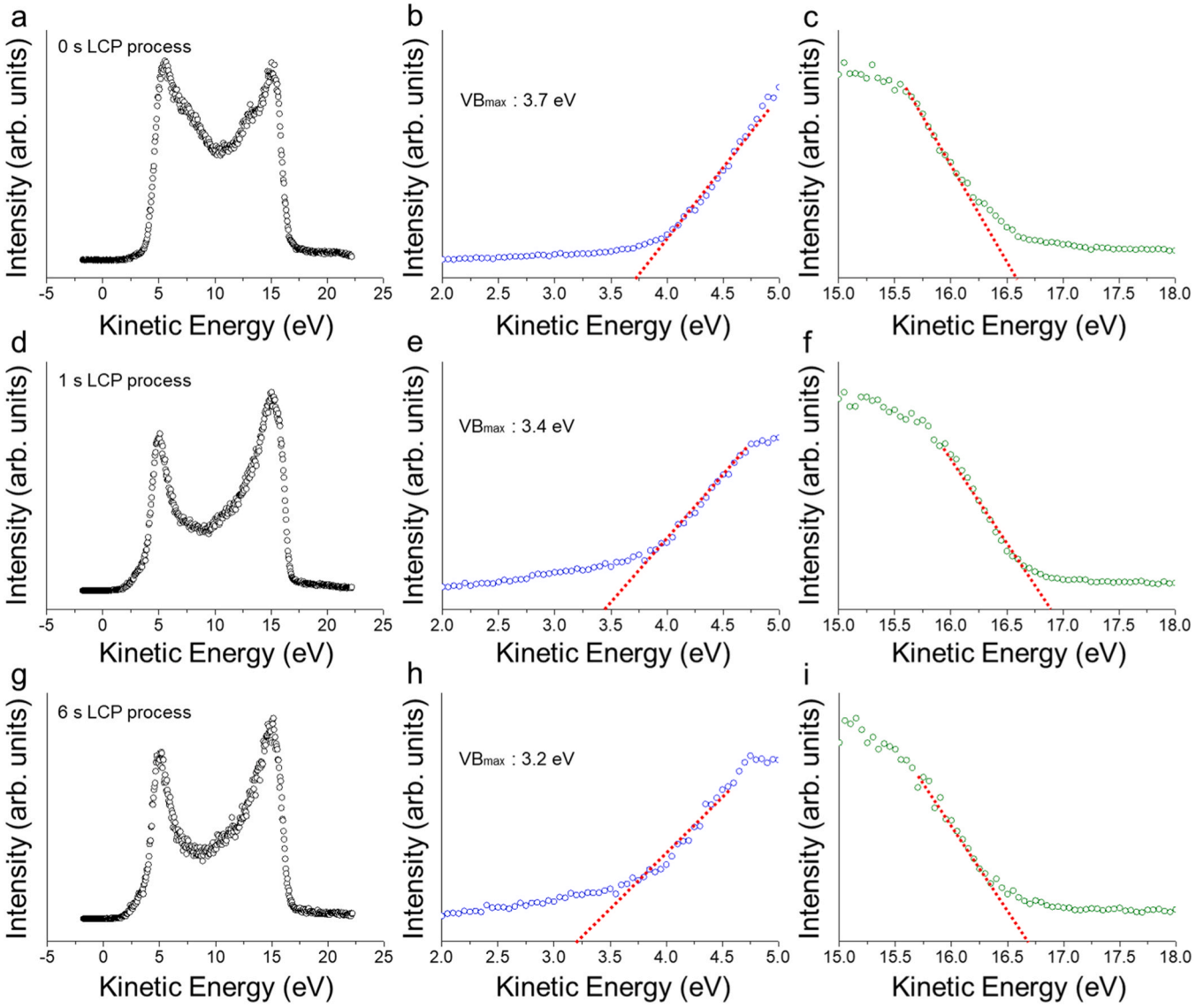

Fig. 8. Energy change in SnO2 NRs according to LCP process. (a) UPS of bare SnO2 NRs, (b) valence band maximum of 3.7 eV, and (c) energy(cut-off) of 16.6 eV for work function of 4.6 eV in bare SnO2 NRs (i.e., 21.2 eV(incident energy) – 16.6 eV). (d) UPS of SnOx NBs + NRs with 1s LCP process, (e) valence band maximum of 3.4 eV, and (f) energy(cut-off) of 16.9 eV for work function of 4.3 eV in SnOx NBs + NRs with 1s LCP process (i.e., 21.2 eV(incident energy) – 16.9 eV). (g) UPS of SnOx NBs + NRs with 6s LCP process, (h) valence band maximum of 3.2 eV, and (i) energy(cut-off) of 16.7 eV for work function of 4.5 eV in SnOx NBs + NRs with 6s LCP process (i.e., 21.2 eV(incident energy) – 16.7 eV).

4.5 eV by the relationship of 21.2 eV (incident energy) – 16.7 eV (Fig. 8i). This implies that despite the short-term and localised effects of the LCP, not only physical changes in shape but also chemical changes on the surface occurred simultaneously.

In most cases, gas sensing in a metal oxide semiconductor nanostructure can be largely divided into (1) semiconductor and oxygen gas, and (2) semiconductor-oxygen gas-target gas (or semiconductor-target gas). First, oxygen adsorption was unavoidable near the semiconductor sample. In general, because the electron affinity of oxygen is greater than that of semiconducting metal oxides, electrons are removed from the surface of the semiconductor and the surface of oxygen is negatively charged with oxygen ions. However, the form of oxygen varies according to the temperature as follows [74,75]:

$$O2(gas) \leftrightarrow O2(ads) \quad (1)$$

$$O2(ads) + e- \rightarrow O2-(ads)\ (T < 100\ ^{\circ}C) \quad (2)$$

$$O2-(ads) + 2e- \rightarrow 2\ O-(ads)\ (100\ ^{\circ}C < T < 300\ ^{\circ}C) \quad (3)$$

$$O-(ads) + e- \rightarrow O2-(ads)\ (T > 300\ ^{\circ}C) \quad (4)$$

As seen above, oxygen plays a role in taking away electrons in the temperature range of 300 °C from room temperature. Because the charge on the semiconductor surface is removed, electrons escape near the semiconductor surface, and an electron-depletion layer (EDL) [76] is naturally formed. In conjunction with this, a conductive channelling width (CCW) consisting of mobile carriers, such as electrons and holes, is created at the bottom of the EDL. If the semiconductor is n-type with many electrons, oxygen is adsorbed, and electrons, which are major carriers, are removed, the EDL on the surface is relatively widened, and the number of electrons in the CCW decreases. Therefore, the resistance increases compared with that before the adsorption of oxygen [77]. However, if the p-type semiconductor has many holes, oxygen is adsorbed, and electrons, which are minor carriers, are removed, the EDL on the surface is relatively widened and the number of holes in the CCW increases. Therefore, the resistance decreases compared with that before

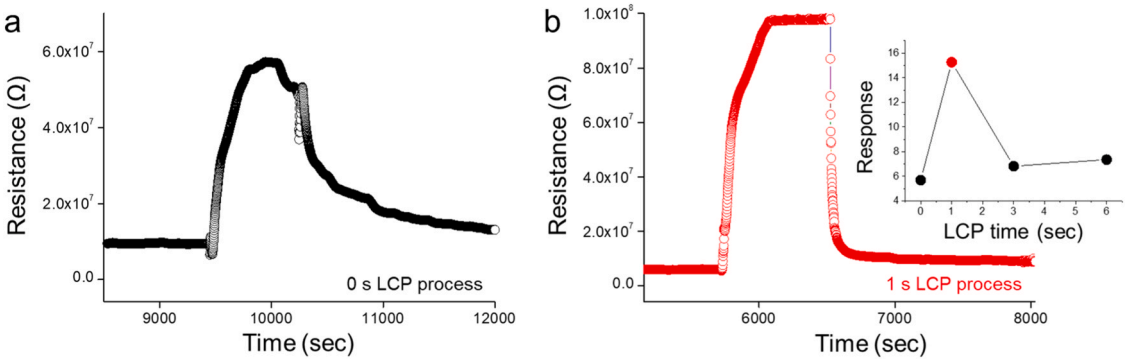

Fig. 9. Dynamic resistance curve of (a) bare SnO2 NRs and (b) SnOx NBs + NRs with 1s LCP process to 50 ppm NO2 gas at 300 °C. The inset of (b) shows the response curve in the 0, 1, 3, 6s LCP process.

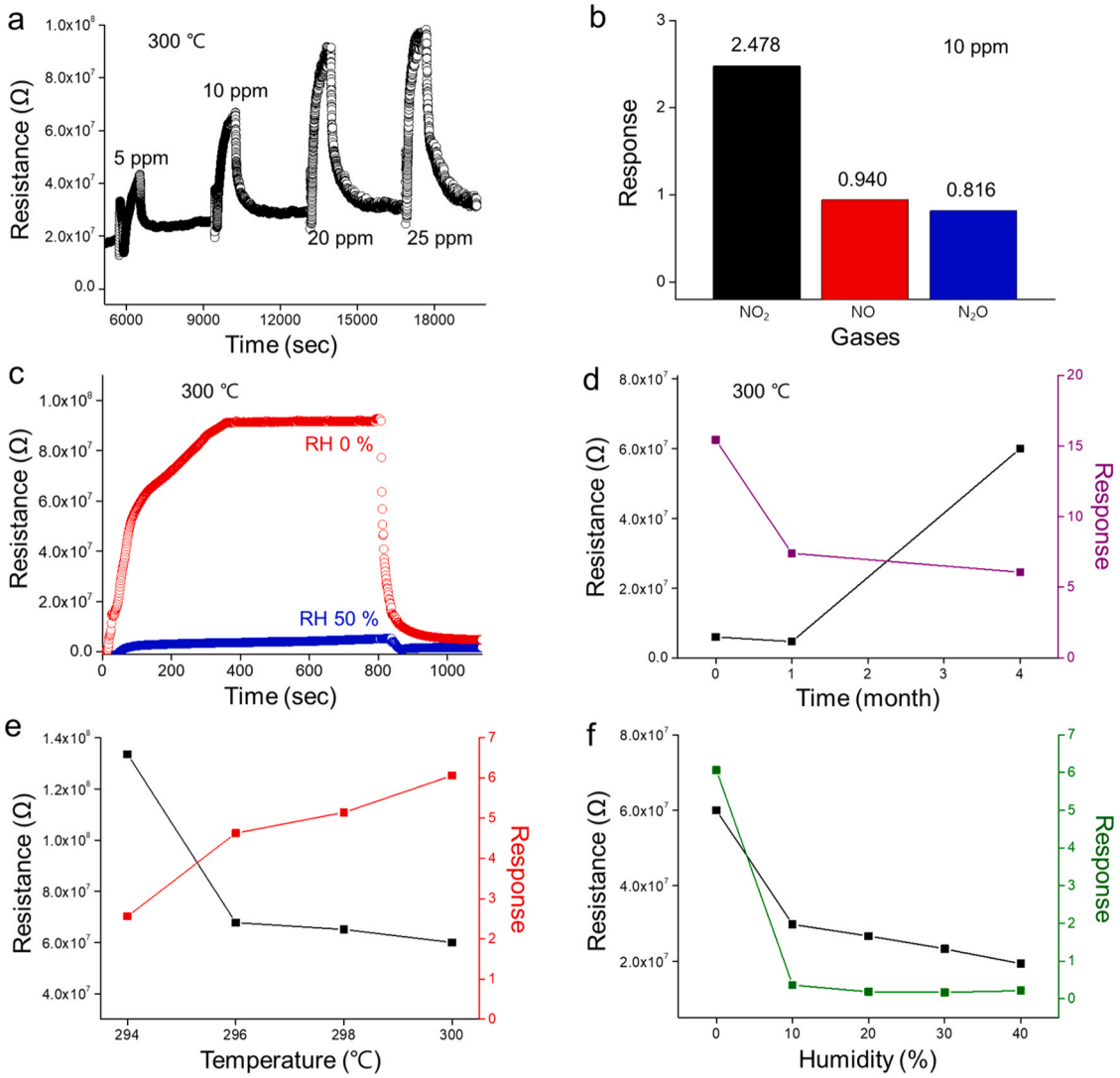

Fig. 10. Comparison of gas sensing performance according to each process variable in SnOx NBs + NRs with 1s LCP process. (a) variation in resistance at NO2 concentration ranges of 5–25 ppm, (b) selectivity test under the same N-O bonding, (c) humidity effect under dry and RH 50 % humid atmosphere. The humid conditions were measured at 22 °C. Therefore, NO2 gas containing 50 % RH prepared at 22 °C was injected, (d) changes in initial resistance and response in long-term stability after one month and four months, (e) variation in initial resistance and response around 300 °C after four months, (d) variation in initial resistance and response below RH 50 % after four months.

the adsorption of oxygen [78]. In the second case, the reaction between the semiconductor, oxygen gas, and target gas (or the semiconductor and target gas) can be considered. Generally, a target gas can be divided into oxidising gas (a gas that oxidises a semiconductor and itself is reduced) and reducing gas (a gas that reduces a semiconductor and itself is oxidised). For the target gas to react, it must be positively or

negatively charged, and temperature helps accelerate the ionic species of the target gas. For example, in the case of an oxidising gas, in the surface adsorption reaction with SnO2 NRs, it plays a role in removing electrons in the SnO2 NRs, eventually widening the EDL of the initial surface while reducing the number of carriers in the CCW; thus, the resistance response eventually increases. On the other hand, in the case of the reducing gas, on the contrary, it plays the role of supplying electrons to SnO2 NRs, rather than reducing the EDL of the initial surface and increasing the number of carriers in the CCW, so the resistance response eventually decreases.

In the case of NO2, it corresponds to an oxidising gas [79,80], and as shown in Fig. 9a, at a concentration of 50 ppm NO2 gas at 300 °C, the resistance increases based on the relationship between the EDL and CCW mentioned above. In the samples where 1, 3, and 6s LCP process were applied (inset of Fig. 9b), the 1s LCP process showed the largest change in resistance (Fig. 9b). In other words, it changed to 5.14, 15.26, 6.82, and 7.35 (inset of Fig. 9b). The corresponding responses, response times, and recovery times are listed in Table S1. At this time, because NO2 gas can be easily ionised, as shown below, electrons, which are the main carriers, can smoothly move from the SnO2 NRs or SnOx NBs + NRs to the NO2 target gas [81,82].

$$NO2(gas) + e- \rightarrow NO2-(ads) \quad (5)$$

$$NO2(gas) + e- \rightarrow NO(gas) + O-(ads) \quad (6)$$

$$NO2(gas) + O2-(ads) + 2e- \rightarrow NO2-(ads) + 2O-(ads) \quad (7)$$

$$NO2-(ads) + 2\,O-(ads) + e- \rightarrow NO2(gas) + 2O2-(ads) \quad (8)$$

At this time, oxygen vacancies can have a greater impact on the sensing response by causing more electron carriers to participate in the target gas and on the surface of the n-type SnO2 sample. In contrast, chemisorbed oxygen reduces the number of electron carriers involved in the target gas and sample surface, resulting in a smaller sensing response. The sample obtained using the 6s LCP process, in particular, displays the shortest response and recovery times because a large amount of stable chemisorbed oxygen is already generated on the SnO2 surface. Hence, the frequency with which unstable NO2 ions can chemically react is relatively small (Table S1). In short, regardless of the number and distribution of SnO2 NBs on the SnO2 NRs surface, the gas-sensing performance was determined by whether the oxygen vacancies or chemisorbed oxygen atoms increased in the existing Sn-O bond.

Fig. 10 shows the concentration, various gases, humidity, and long-term stability trends of SnOx NBs + NRs with a 1s LCP process, which is the best process condition. Even in the low-concentration region (< 50 ppm NO2 gas), the higher the concentration, the larger the response obtained (Fig. 10a and SI, Table S2), which means that there is sufficient room for the target gas molecules to adsorb on the surface of the SnO2 NRs or SnOx NBs + NRs. In case of selectivity, NO2 gas has a higher selectivity than the other gases because it has a smaller bonding energy [83]. In addition, even for the same N-O bonding, a stronger response was observed at a gas concentration of 10 ppm (Fig. 10b). The gas-sensing characteristics of gases without N–O bonds were also investigated (SI, Fig. S4). The resistance decreases rapidly when isoprene gas is adsorbed (Fig. S4a) but ultimately does not recover for >2500 s, and acetone gas (SI, Fig. S4b) also exhibits the disadvantage of an extended recovery time, unlike the rapid change in resistance. In contrast, H2 gas (SI, Fig. S4c) displays a shorter recovery time than those of the above gases, but the response (i.e. 10.12) is lower than that (i.e.

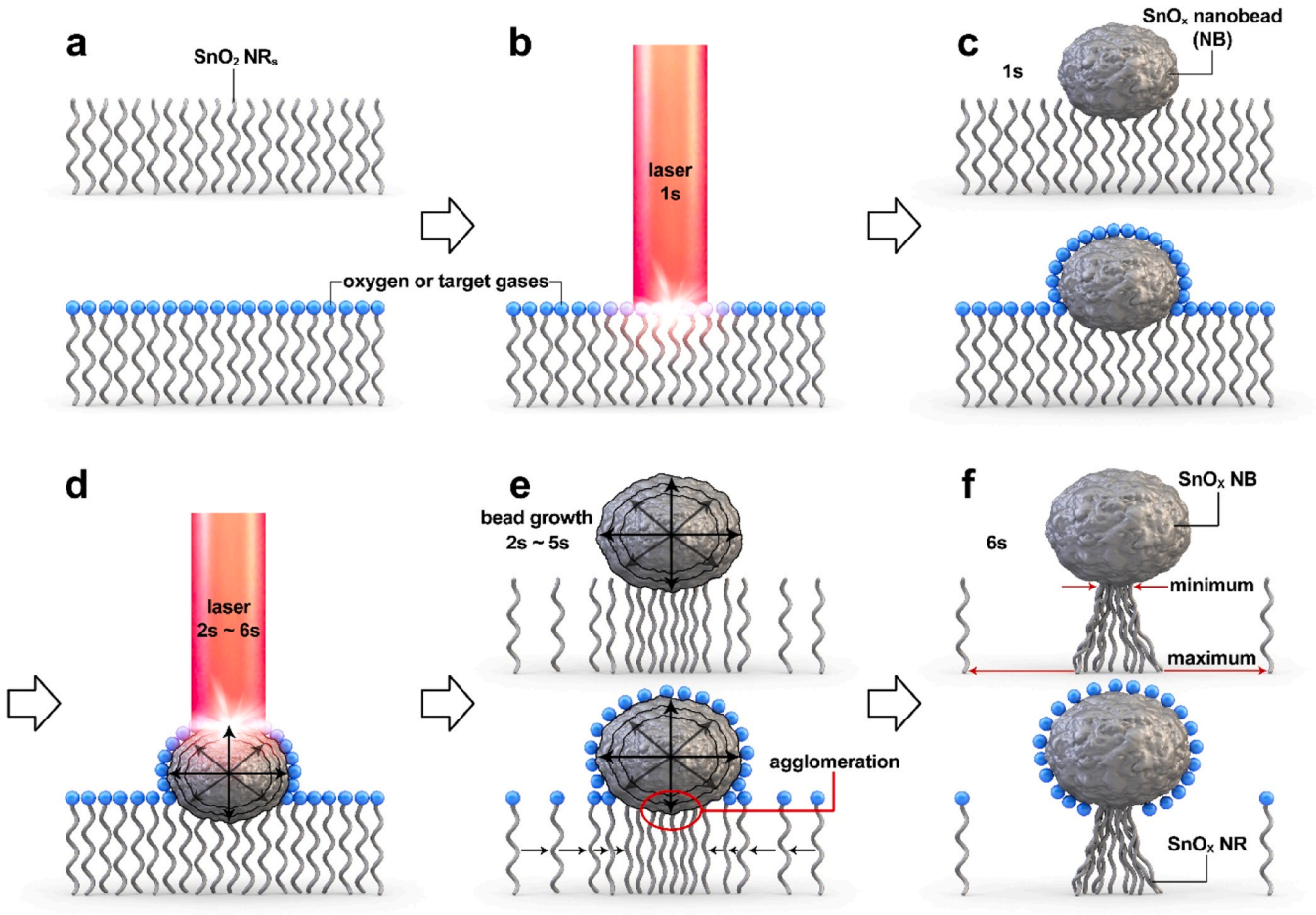

Fig. 11. Schematic diagram showing changes in morphology and CSA of bare SnO2 NRs as the LCP process time increases.

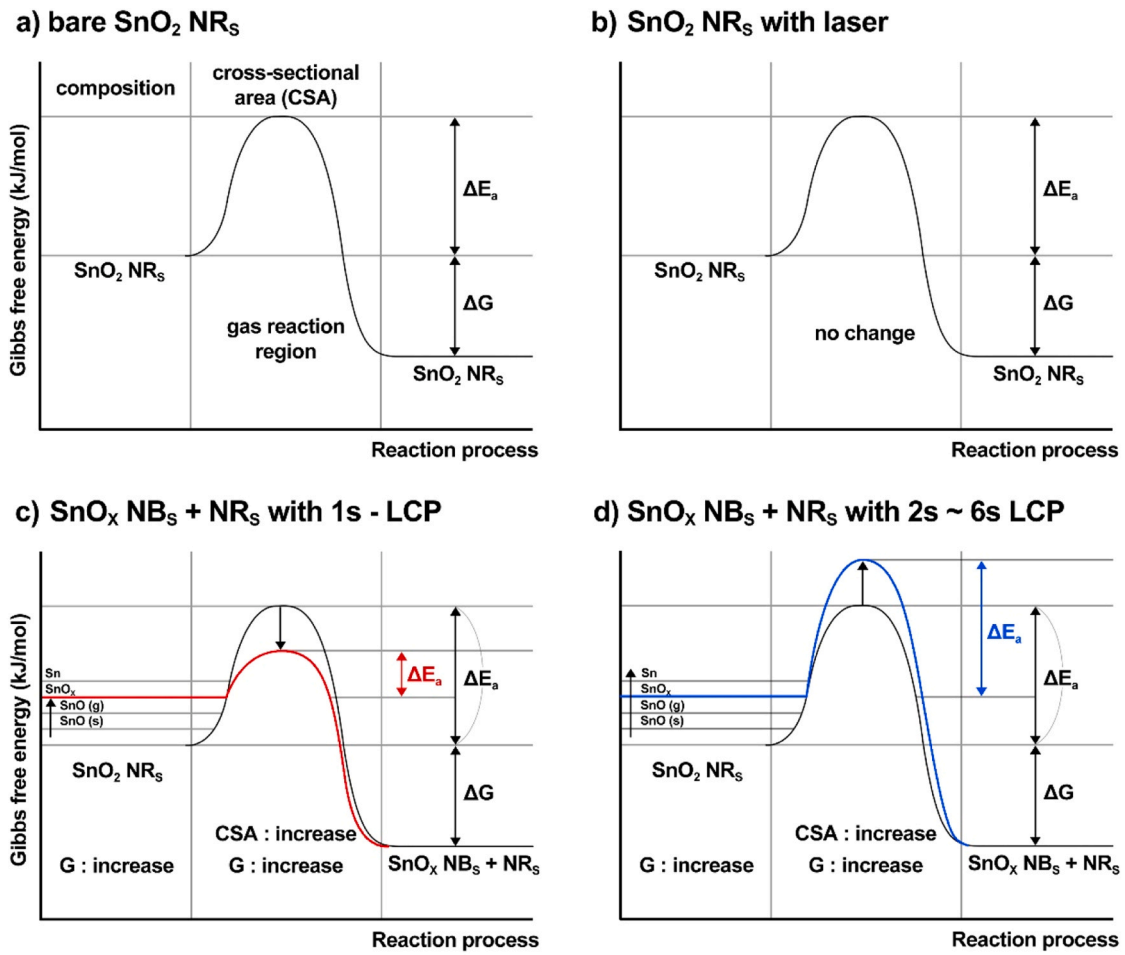

Fig. 12. Gibbs free energy and activation energy depending on the degree of LCP process in gas sensing. (a) Bare SnO2 NRs. (b) SnO2 NRs with laser. (c) SnOx NBs + NRs with 1s LCP process. (d) SnOx NBs + NRs with 2–6s LCP process.

15.26) of NO2 gas. No special tendencies are observed for other gases, and significant differences are observed depending on the chemical properties of each gas. Compared with the dry state, the response decreased when the RH was higher (50 %) (Fig. 10c). This is because the humidity in the air is already adsorbed on the surface of the sample before the target gas is adsorbed, which can hinder the movement of the target gas and the mobile carrier of the sample [84,85]. In addition, the influence of humidity also results from the main gas-sensing mechanism analysed from XPS. For example, when the humidity around the sample increases, it corresponds to an increase in the amount of oxygen, similar to the effect observed in the 3s and 6s LCP processes, which rapidly reduces the number of electrons on the n-type SnO2 surface. In other words, humidity reduces the number of oxygen vacancies formed on the surface and increases the amount of chemisorbed oxygen. Similarly, the decrease in the response of the sample after one month and four months was also partially affected by humidity (Fig. 10d). To yield more detailed data, the SnO2 NRs obtained via the 1s LCP process were analysed using EDX (SI, Fig. S5a) and XPS (SI, Fig. S5b) after one month to investigate the cause of the deterioration in gas sensing. The number of oxygen vacancies in the sample is significantly reduced. Instead, similar to the sample obtained using the 6s LCP process, increases in the amounts of oxidation due to natural oxidation (SI, Fig. S5a) and oxygen-based chemisorbed oxygen are observed (Sn4+ > Sn2+, SI, Fig. S5b). The effects of temperature and humidity on long-term stability were further analysed. In a sensing test near a temperature of 300 °C, the greatest response was obtained at 300 °C, where the number of mobile carriers increases as the temperature increases. And as the temperature increased, the initial resistance decreased (Fig. 10e). Therefore, it was possible to obtain a relationship between the sensing improvement effect of 927 ppb of NO2 per 1 °C temperature in the process temperature range. In the range below RH 50 %, both initial resistance and response decrease each time RH increases by 10 %, but the greatest decrease was observed in the initial RH 10 % range (Fig. 10 f). Therefore, for every RH 1 %, there is a correlation of 506 ppb of NO2 reduction effect.

Considering the simplicity and efficiency of the proposed LCP process, it is worth continuing research in the future.

First, regarding the surface defects of SnO2 NRs, various types of point defects may exist in SnO2. Xiong et al. [86] classified 17 types of surface defects that could affect the gas sensing of SnO2, including oxygen vacancies, double-ionised oxygen vacancies, tin antisites, bridging oxygen vacancies, and Sn4+–oxygen vacancy associates among others. The defect engineering strategies that can form these defects are largely divided into irradiation, heat treatment, chemical reduction, tailoring of specially exposed facets, and doping. In particular, it has been reported that, while other methods (i.e. irradiation, heat treatment, tailoring specially exposed facets, and doping) form various defects, only oxygen vacancies are formed in the case of chemical reduction, which has the advantage of being simple and easy without the need for high temperatures. At this time, our defect formation method is different from the above defect formation method, and this contributes to inducing different Sn–O bonds on the surface of the SnO2 NRs depending on the applied time. In other words, under the 1s LCP process, the bindings of Sn-O are broken and O vacancies are mainly formed, whereas under the 3s and 6s LCP processes, as the laser is concentrated, the temperature rises around that area, and oxygen gathers from the surrounding area to that area, resulting in the formation of more chemisorbed oxygen than

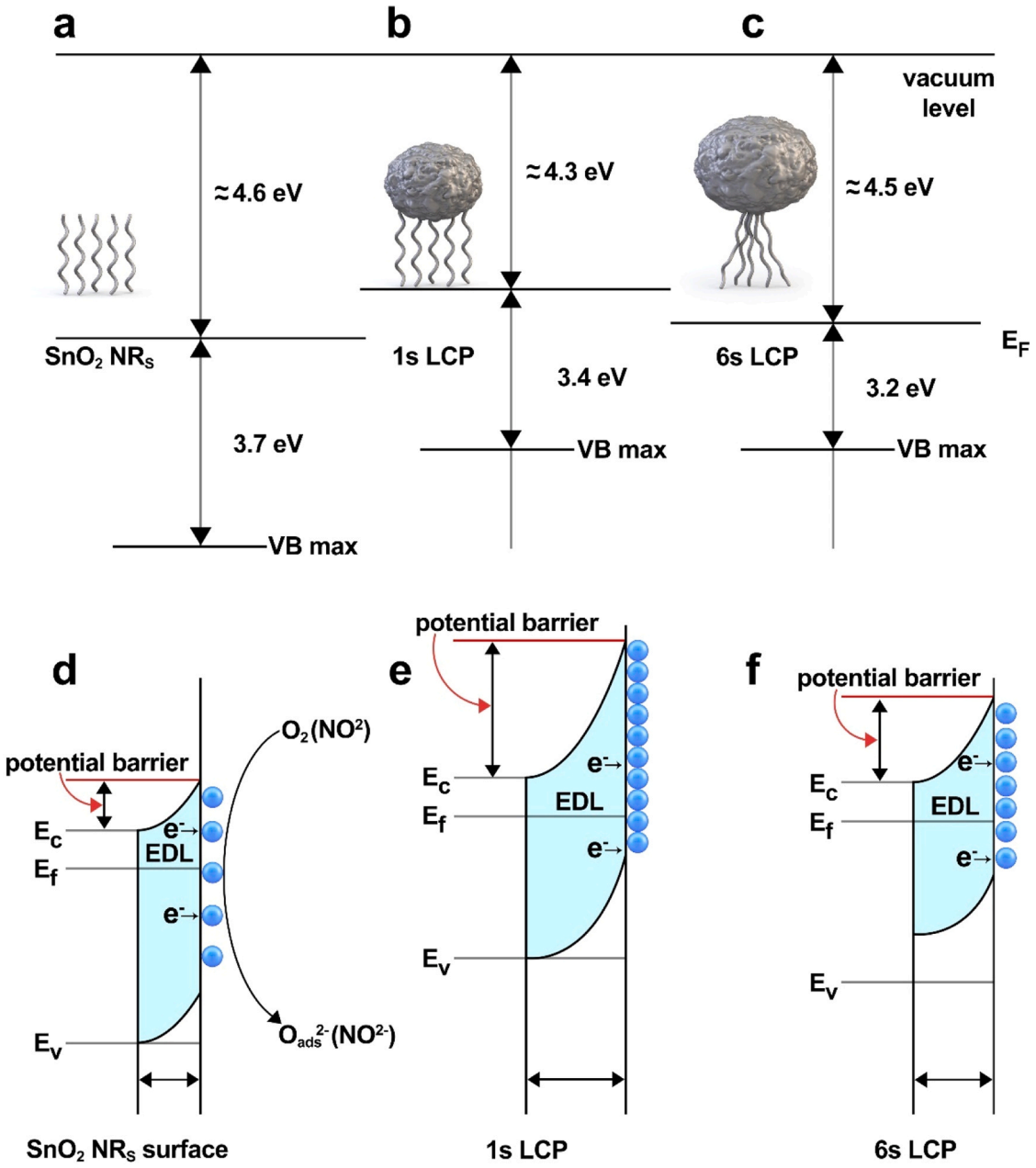

Fig. 13. Change in valence band maximum and surface potential with LCP process time. (a, d) Bare SnO2 NRs. (b, e) SnOx NBs + NRs with 1s LCP process. (c, f) SnOx NBs + NRs with 6s LCP process.

the existing Sn-O bond. In this process, even if there is no clear change in shape, such as in the case of SnO2 NBs, changes in the surface composition can occur to some extent in all areas where the laser is focused. In other words, compared to bare SnO2, in the 1s LCP process, a reduction reaction occurs with a smaller amount of oxygen, such as oxygen vacancies, and in the 3s and 6s LCP processes, an oxidation reaction occurs with a larger amount of oxygen, such as chemisorbed oxygen. As seen in other research results [86], these oxygen vacancies are so overwhelming that they account for 70 of 85 cases; therefore, they can be the main mechanism of the n-type SnO2 surface reaction.

Based on the specific surface areas (SI, Fig. S3), the mechanism by which the CSA adsorbed by the increases in the target gas can be explained as shown in Fig. 11. In the case of SnO2 NRs, there are sites where oxygen in air or the target gas can be adsorbed on the edge surface of each NRs (Fig. 11a). However, if the 1s LCP process is added at this time (Fig. 11b), the CSA where gases can be adsorbed increases as the surfaces are agglomerated into SnOx NBs in the area where the laser is focused (Fig. 11c). When a longer LCP process was applied (2–6s) (Fig. 11d), the SnOx NRs congregated beneath the SnOx NBs rather than growing. Therefore, the total CSA of the SnOx NBs + NRs in Fig. 11e was lower than that of the SnOx NBs + NRs, as shown in Fig. 11c. Therefore, the 6s LCP process (Fig. 11d and f) demonstrates a much smaller response than that shown in Fig. 11c.

This can be understood more easily using the thermodynamic data (Fig. 12 and Table S3). Fig. 12a shows the Gibbs free energy of the bare SnO2 NRs before and after the NO2 gas reaction. The activation energy of ΔEa here includes the factor of how efficiently the target gas can be adsorbed on the adsorption surface, and it can be said to be directly related to the total CSA of SnO2 NRs mentioned in Fig. 11. When only the laser was applied to the bare SnO2 NRs, there was no significant change in ΔEa (Fig. 12b and SI, Fig. S2). However, when the 1s LCP process was applied (Fig. 12c), the existing SnO2 NRs gradually reduced

and moved toward SnO and Sn, and the Gibbs free energy of the reactants became higher than that of the initial SnO2 NRs [87]. In addition, SnOx NBs + NRs formed even in the section where the reaction of the target gas occurred, and the total CSA was much wider than before, which can play a role in lowering the activation energy required for gas-sensing reactions. In other words, a synergistic effect can be achieved by increasing the initial Gibbs free energy and reducing the activation energy. As mentioned above, the effect of the composition change was a much more dominant factor than that of the CSA. However, when the LCP process time was increased from 1 to 2–6s (Fig. 12d), the total CSA decreased rather than increasing the Gibbs free energy of the initial reactant. In addition, the oxidation reactions of Sn and O occur actively on the surface. Eventually, the effect of increasing the activation energy increased, and eventually, the gas-sensing response decreased.

Therefore, the gas-sensing mechanism based on the LCP process can be organised as shown in Fig. 13. SnO2 NRs with a work function of 4.6 eV and a valence band maximum of 3.7 eV adsorb oxygen gas or target gas on the surface, and an EDL was formed near the surface (Fig. 13a and d). In the case of the 1s LCP process, as the existing SnO2 NRs aggregated, the largest CSA of SnOx NBs + NRs could be adsorbed by the gas formed. And at the same time the reduction reaction of Sn-O occurs, leading to changes in the work function and valence band maximum to 4.3 eV and 3.4 eV, respectively (Fig. 13b). Eventually, as shown in Fig. 13e, as the EDL widened, the potential barrier increased, resulting in an increase in the gas-sensing resistance. However, in the case of the 6s LCP process, the CSA of the SnOx NBs + NRs decreased. At the same time the oxidation reaction of Sn-O occurs predominantly indicating the work function and valence band maximum changed to 4.5 eV and 3.2 eV, respectively (Fig. 13c). In the energy band of this state, the gas-sensing response decreased (Fig. 13 f). However, the effect of this cross-sectional area can be considered to be minimal for gas sensing. Therefore, as in the XPS results mentioned above (Figs. 6–7), it is necessary to determine where the formation of different potential barriers originates compared to bare SnO2 NRs, depending on the LCP conditions. Ultimately, it must be approached according to the type of chemical bonding on the surface. Therefore, the 1s LCP process can cause the reduction of Sn-O and induce many oxygen vacancies on the surface of the SnO2 NRs (Fig. 13b and e), and the 6s LCP process can cause the oxidation of Sn-O and induce chemisorbed oxygen on the surface of the SnO2 NRs (Fig. 13c and f).

As mentioned above, the LCP process is a new technique and follow-up studies are being performed.

4. Conclusions

The surface morphology and composition of the SnO2 NRs synthesised using the GLAD method could be easily controlled using a high-energy laser beam. The proposed LCP method was able to determine the size and composition of the SnOx NBs in the condensed area, especially within a few seconds. Therefore, by sequentially applying LCP, under the condition of 1s LCP, the response to NO2 gas was increased by approximately three times compared to that of bare SnO2 NRs, and based on this, a gas-sensing mechanism using the relationship between the reduction and oxidation on the surface was introduced. The effectiveness of LCP was demonstrated using the effect of changing the thermodynamic composition during gas sensing. With LCP outperforming other processes in terms of equipment, pre- and post-treatment, process temperature, process time, and vacuum degree, it is expected to be further researched for various applications in the future.

CRediT authorship contribution statement

Changhyun Jin: Conceptualization, Investigation, Visualization, Data curation, Writing - original draft. **Hyunseong Yang:** Conceptualization, Investigation, Visualization, Data curation. **Taewon Lim:** Investigation, Data curation. **Kyu Hyoung Lee:** Supervision, Project administration, Writing - review & editing. **Wooyoung Lee:** Supervision, Project administration, Writing - review & editing.

Declaration of Competing Interest

The authors declare that they have no known competing financial interests or personal relationships that could have appeared to influence the work reported in this paper.

Data availability

Data will be made available on request.

Acknowledgements

This work was supported by the Technology Innovation Program (‘20013621’, Center for Super Critical Material Industrial Technology) funded By the Ministry of Trade, Industry & Energy (MOTIE, Korea). This research was supported by the National Research Foundation of Korea (NRF) grant funded by the Korea government (MIST) (No. NRF-2022M3H4A3053304, National Core Materials Research Center (Platform type)). This research was supported by the Basic Science Research Program through the National Research Foundation of Korea (NRF) funded by the Ministry of Education (NRF-2019R1A6A1A11055660 and RS-2023-00243422). Changhyun Jin was supported by the Korea Initiative for fostering University of Research and Innovation (KIURI) Program of the National Research Foundation (NRF) funded by the Korean government (MSIT) (NRF-2020M3H1A1077207).

Appendix B. Supporting information

Supplementary data associated with this article can be found in the online version at doi:10.1016/j.snb.2024.136170.

References

[1] M.A. Han, H.-J. Kim, H.C. Lee, J.-S. Park, H.-N. Lee, Effects of porosity and particle size on the gas sensing properties of SnO2 films, Appl. Surf. Sci. 481 (2019) 133–137.
[2] P.G. Choi, N. Izu, N. Shirahata, Y. Masuda, Improvement of sensing properties for SnO2 gas sensor by tuning of exposed crystal face, Sens. Actuators B Chem. 296 (2019) 126655.
[3] D. An, N. Liu, H. Zhang, Q. Sun, C. Li, Y. Li, Q. Zhang, Y. Lu, Enhanced n-butanol sensing performance of SnO2-based gas sensors by doping In2O3 via co-precipitation method, Sens. Actuators B Chem. 340 (2021) 129944.
[4] K.-R. Park, H.-B. Cho, J. Lee, Y. Song, W.-B. Kim, Y.-H. Choa, Design of highly porous SnO2-CuO nanotubes for enhancing H2S gas sensor performance, Sens. Actuators B Chem. 302 (2020) 127179.
[5] H. Xiang, Y. Long, X. Yu, X. Zhang, N. Zhao, J. Xu, A novel and facile method to prepare porous hollow CuO and Cu nanofibers based on electrospinning, Crystengcomm 13 (2011) 4856–4860.
[6] Z. Cui, X. Wang, Y. Ding, E. Li, K. Bai, J. Zheng, T. Liu, Adsorption of CO, NH3, NO, and NO2 on pristine and defective g-GaN: Improved gas sensing and functionalization, Appl. Surf. Sci. 530 (2020) 147275.
[7] M.J. Kang, E.S. Hwang, M. Kim, T.S. Park, S.T. Shin, B.-H. Cheong, Enhancement of ultra-violet light absorption of surface-textured silicon induced by nanosecond laser irradiations, Appl. Surf. Sci. 530 (2020) 147260.
[8] J.-C. Lim, C. Jin, M.S. Choi, M.Y. Kim, S. Kim, S.-M. Choi, S.-H. Baek, K.H. Lee, H.-S. Kim, Synthesis, morphology, characterisation, and ethanol gas sensing of hierarchical flower-like Co-doped WO3 nanoplates by solvothermal route, Ceram. Int. 47 (2021) 20956–20964.
[9] S.-W. Choi, C. Jin, Temperature-dependent selectivity of bead-like TeO2 nanostructured gas sensors, RSC Adv. 5 (2015) 71955–71960.
[10] X. Han, M. Jin, S. Xie, Q. Kuang, Z. Jiang, Y. Jiang, Z. Xie, L. Zheng, Synthesis of tin dioxide octahedral nanoparticles with exposed high-energy {221} facets and enhanced gas-sensing properties, Angew. Chem.-Int. Edit 48 (2009) 9180–9183.
[11] T. Mokoena, H.C. Swart, K.T. Hillie, Z.P. Tshabalala, M. Jozela, J. Tshilongo, D. E. Motaung, Enhanced propanol gas sensing performance of p-type NiO gas sensor induced by exceptionally large surface area and crystallinity, Appl. Surf. Sci. 571 (2022) 151121.
[12] Z.P. Tshabalala, T.P. Mokoena, K.T. Hillie, H.C. Swart, D.E. Motaung, Improved BTEX gas sensing characteristics of thermally treated TiO2 hierarchical spheres manifested by high-energy {001} crystal facets, Sens. Actuators B Chem. 338 (2021) 129774.

[13] G. Korotcenkov, Metal oxides for solid-state gas sensors: What determines our choice? Mater. Sci. Eng. B 139 (2007) 1–23.
[14] D. Effect, S. Tsiulyanu, H.D. Liess Marian, I. Eisele, Effect of annealing and temperature on the NO2 sensing properties of tellurium based films, Sens. Actuators B Chem. 100 (2004) 380–386.
[15] X.-Y. Huang, Z.-T. Chi, J. Liu, D.-H. Li, X.-J. Sun, C. Yan, Y.-C. Wang, H. Li, X.-D. Wang, W.-F. Xie, Enhanced gas sensing performance based on p-NiS/n-In2O3 heterojunction nanocomposites, Sens. Actuators B Chem. 304 (2020) 127305.
[16] Y. Yan, J. Liu, H. Zhang, D. Song, J. Li, P. Yang, M. Zhang, J. Wang, One-pot synthesis of cubic ZnSnO3/ZnO heterostructure composite and enhanced gas-sensing performance, J. Alloy. Compd. 780 (2019) 193–201.
[17] J. Zhao, C. Xie, L. Yang, S. Zhang, G. Zhang, Z. Cai, Enhanced gas sensing performance of Li-doped ZnO nanoparticle film by the synergistic effect of oxygen interstitials and oxygen vacancies, Appl. Surf. Sci. 330 (2015) 126–133.
[18] M. Al-Hashem, S. Akbar, P. Morris, Role of oxygen vacancies in nanostructured metal-oxide gas sensors: a review, Sens. Actuators B Chem. 301 (2019) 126845.
[19] C.H. Cho, J.Y. Oh, T.I. Lee, Two-dimensional self-assembled network structure of Co3O4 quantum-dot-decorated ZnO nanobeads for ppb-level acetone sensors, Mater. Lett. 314 (2022) 131826.
[20] Y. Kabe, S. Sakamoto, M. Hatakeyama, Y. Yamaguchi, M. Suematsu, M. Itonaga, H. Handa, Application of high-performance magnetic nanobeads to biological sensing devices, Anal. Bioanal. Chem. 411 (2019) 1825–1837.
[21] P. Karen, Crystal structure and oxygen nonstoichiometry of ErBa2Fe3O8, J. Solid State Chem. 322 (2023) 123953.
[22] M.U. Abulkhaev, M.S. Molokeev, A.S. Oreshonkov, A.S. Aleksandrovsky, A. V. Kertman, D.N. Kamaev, O.V. Trofimova, A.V. Elyshev, O.V. Andreev, Properties of GdSF and phase diagram of the GdF3 - Gd2S3 system, J. Solid State Chem. 322 (2023) 123991.
[23] L. Wang, S. Chen, W. Li, K. Wang, Z. Lou, G. Shen, Grain-boundary-induced drastic sensing performance enhancement of polycrystalline-microwire printed gas sensors, Adv. Mater. 31 (2019) 1804583.
[24] H. Jiang, W. Hu, The emergence of organic single-crystal electronics, Angew. Chem. -Int. Ed. 59 (2020) 1408–1428.
[25] M.S. Choi, A. Mirzaei, H.G. Na, S. Kim, D.E. Kim, K.H. Lee, C. Jin, S.-W. Choi, Facile and fast decoration of SnO2 nanowires with Pd embedded SnO2-x nanoparticles for selective NO2 gas sensing, Sens. Actuators B Chem. 340 (2021) 129984.
[26] M.S. Choi, H.G. Na, J.H. Bang, A. Mirzaei, S. Han, H.Y. Lee, S.S. Kim, H.W. Kim, C. Jin, SnO2 nanowires decorated by insulating amorphous carbon layers for improved room-temperature NO2 sensing, Sens. Actuators B Chem. 326 (2021) 128801.
[27] P. Raksa, A. Gardchareon, T. Chairuangsri, P. Mangkorntong, N. Mangkorntong, S. Choopun, Ethanol sensing properties of CuO nanowires prepared by an oxidation reaction, Ceram. Int. 35 (2009) 649–652.
[28] P. Sun, W. Wang, Y. Liu, Y. Sun, J. Ma, G. Lu, Hydrothermal synthesis of 3D urchin-like -Fe2O3 nanostructure for gas sensor, Sens. Actuators B Chem. 173 (2012) 52–57.
[29] Z. Zhang, X. Zou, L. Xu, L. Liao, W. Liu, J. Ho, X. Xiao, C. Jiang, J. Li, Hydrogen gas sensor based on metal oxide nanoparticles decorated graphene transistor, Nanoscale 7 (2015) 10078–10084.
[30] H.-I. Chen, C.-Y. Hsiao, W.-C. Chen, C.-H. Chang, T.-C. Chou, I.-P. Liu, K.-W. Lin, W.-C. Liu, Characteristics of a Pt/NiO thin film-based ammonia gas sensor, Sens. Actuators B Chem. 256 (2018) 962–967.
[31] H. Liu, W. Shen, X. Chen, J.-P. Corriou, A high-performance NH3 gas sensor based on TiO2 quantum dot clusters with ppb level detection limit at room temperature, J. Mater. Sci. Mater. Electron 29 (2018) 18380–18387.
[32] Q. Yang, Y. Wang, J. Liu, J. Liu, Y. Gao, P. Sun, Z. Jie, T. Zhang, Y. Wang, G. Lu, Enhanced sensing response towards NO2 based on ordered mesoporous Zr-doped In2O3 with low operating temperature, Sens. Actuators B Chem. 241 (2017) 806–813.
[33] J.B. Cui, L.Q. Shi, T.F. Xie, D.J. Wang, Y.H. Lin, UV-light illumination room temperature HCHO gas-sensing mechanism of ZnO with different nanostructures, Sens. Actuators B Chem. 227 (2016) 220–226.
[34] X.S. Liang, G.X. Jin, F.M. Liu, X.S. Zhang, S.S. An, J. Ma, G.Y. Lu, Synthesis of In2O3 hollow nanofibers and their application in highly sensitive detection of acetone, Ceram. Int. 41 (2015) 13780–13787.
[35] S. Wang, J. Cao, W. Cui, L. Fan, X. Li, D. Li, T. Zhang, One-dimensional porous Co3O4 rectangular rods for enhanced acetone gas sensing properties, Sens. Actuators B Chem. 297 (2019) 126746.
[36] P.M. Bulemo, D.-H. Kim, I.-D. Kim, Controlled synthesis of electrospun hollow Pt-loaded SnO2 microbelts for acetone sensing, Sens. Actuators B Chem. 344 (2021) 130208.
[37] S. An, S. Park, H. Ko, C. Jin, W.I. Lee, C. Lee, Enhanced ethanol sensing properties of multiple networked Au-doped In2O3 nanotube sensors, J. Phys. Chem. Solids 74 (2013) 979.
[38] S. Bai, S. Chen, L. Chen, K. Zhang, R. Luo, D. Li, C.C. Liu, Ultrasonic synthesis of MoO3 nanorods and their gas sensing properties, Sens. Actuators B Chem. 174 (2012) 51.
[39] S.-H. Huang, D. Susanti, D.-S. Tsai, Y.-C. Hsieh, Y.-S. Huang, W.-H. Chung, Structures and catalytic properties of PtRu electrocatalysts prepared via the reduced RuO2 nanorods array, Langmuir 24 (2008) 2785–2791.
[40] M. Plodinec, I. Grčić, M.G. Willinger, A. Hammud, X. Huang, I. Panžić, A. Gajović, Black TiO2 nanotube arrays decorated with Ag nanoparticles for enhanced visible-light photocatalytic oxidation of salicylic acid, J. Alloy. Compd. 776 (2019) 883–896.
[41] J. Kukkola, M. Mohl, A.R. Leino, J. Mäklin, N. Halonen, A. Shchukarew, Z. Konya, H. Jantunen, K. Lirdas, Room temperature hydrogen sensors based on metal decorated WO3 nanowires, Sens. Actuators B Chem. 186 (2013) 90–95.
[42] G. Lei, C. Lou, X. Liu, J. Xie, Z. Li, W. Zheng, J. Zhang, Thin films of tungsten oxide materials for advanced gas sensors, Sens. Actuators B Chem. 341 (2021) 15.
[43] G.S. Aluri, A. Motayed, A.V. Davydov, V.P. Oleshko, K.A. Bertness, N.A. Sanford, M.V. Rao, Highly selective GaN-nanowire/TiO2-nanocluster hybrid sensors for detection of benzene and related environment pollutants, Nanotechnology 22 (2011) 295503.
[44] G.-J. Sun, H. Kheel, S. Park, S. Lee, S.E. Park, C. Lee, Synthesis of TiO2 nanorods decorated with NiO nanoparticles and their acetone sensing properties, Ceram. Int. 42 (2016) 1063–1069.
[45] X. Chen, Y. Shen, P. Zhou, S. Zhao, X. Zhong, T. Li, C. Han, D. Wei, D. Meng, NO2 sensing properties of one-pot-synthesized ZnO nanowires with Pd functionalization, Sens. Actuators B Chem. 280 (2019) 151–161.
[46] M.R. Mohammadia, D.J. Fray, Development of nanocrystalline TiO2–Er2O3 and TiO2–Ta2O5 thin film gas sensors: controlling the physical and sensing properties, Sens. Actuators B Chem. 141 (2009) 76–84.
[47] S. Bai, D. Li, D. Han, R. Luo, A. Chen, C.L. Chung, Preparation, characterization of WO3-SnO2 nanocomposites and their sensing properties for NO2, Sens. Actuators B Chem. 150 (2010) 749–755.
[48] L.I. Trakhtenberg, G.N. Gerasimov, V.F. Gromov, T.V. Belysheva, O.J. Ilegbusi, Effect of composition and temperature on conductive and sensing properties of CeO2 + In2O3 nanocomposite films, Sens. Actuators B Chem. 209 (2015) 562–569.
[49] T. Wang, B. Liu, Q. Li, S. Wang, Controllable construction of Cr2O3-ZnO hierarchical heterostructures and their formaldehyde gas sensing properties, Mater. Lett. 221 (2018) 260–263.
[50] B. Wang, H.T. Jin, Z.Q. Zheng, Y.H. Zhou, C. Gao, Low-temperature and highly sensitive C2H2 sensor based on Au decorated ZnO/In2O3 belt-tooth shape nano-heterostructures, Sens. Actuators B Chem. 244 (2017) 344–356.
[51] C.-H. Kwak, H.-S. Woo, J.-H. Lee, Selective trimethylamine sensors using Cr2O3-decorated SnO2 nanowires, Sens. Actuators B Chem. 204 (2014) 231–238.
[52] V. Paolucci, G. D'Olimpio, C.-N. Kuo, C.S. Lue, D.W. Boukhvalov, C. Cantalini, A. Politano, Self-assembled SnO2/SnSe2 heterostructures: a suitable platform for ultrasensitive NO2 and H2 sensing, ACS Appl. Mater. Interfaces 12 (2020) 34362–34369.
[53] P. Bisht, A. Kumar, I.T. Jensen, M. Ahmad, B.D. Belle, B.R. Mehta, Enhanced gas sensing response for 2D α-MoO3 layers: Thickness-dependent changes in defect concentration, surface oxygen adsorption, and metal-metal oxide contact, Sens. Actuators B Chem. 341 (2021) 129953.
[54] S. Zhao, Y. Shen, P. Zhou, F. Hao, X. Xu, S. Gao, D. Wei, Y. Ao, Y. Shen, Enhanced NO2 sensing performance of ZnO nanowires functionalized with ultra-fine In2O3 nanoparticles, Sens. Actuators B Chem. 308 (2020) 127729.
[55] S. Shah, S. Han, S. Hussain, G. Liu, T. Shi, A. Shaheen, Z. Xu, M. Wang, G. Qiao, NO2 gas sensing responses of In2O3 nanoparticles decorated on GO nanosheets, Ceram. Int. 9 (2022) 12291–12298.
[56] A. Hermawan, B. Zhang, A. Taufik, Y. Asakura, T. Hasegawa, J. Zhu, P. Shi, S. Yin, CuO nanoparticles/Ti3C2Tx MXene hybrid nanocomposites for detection of toluene gas, ACS Appl. Nano Mater. 3 (2020) 4755–4766.
[57] S. Kim, J.H. Bang, M.S. Choi, W. Oum, A. Mirzaei, N. Lee, H.-C. Kwon, D. Lee, H. Jeon, H.W. Kim, Synthesis, characterization and gas-sensing properties of pristine and SnS2 functionalized TeO2 nanowires, Met. Mater. -Int. 25 (2019) 805–813.
[58] Y.-S. Lin, C.-Y. Wu, F.-M. Pan, J.-T. Sheu, Selective deposition of PdO nanoparticles on Si nanodevices for hydrogen sensing, ACS Appl. Nano Mater. 6 (2023) 10365–10374.
[59] Z.-H. Shi1, Y.-J. Hsiao, S.-C. Wang, W.-C. Tien, InOx doped SnO2 nanostructure deposited on MEMS device by PE-ALD process for detection of NO2, J. Electrochem. Soc. 170 (2023) 027509.
[60] A. Kumar, N. Sharma, A.P. Gutal, D. Kumar, P. Kumar, M. Paranjothy, M. Kumar, Growth and NO2 gas sensing mechanisms of vertically aligned 2D SnS2 flakes by CVD: Experimental and DFT studies, Sens. Actuators B Chem. 353 (2022) 131078.
[61] J.-H. Choi, M.-J. Ha, D.G. Kim, J.-M. Lee, J.-H. Ahn, Low-temperature growth of 2D-MoS2 thin films by plasma-enhanced atomic layer deposition using a new molybdenum precursor and applicability to gas sensors, ACS Appl. Nano Mater. 6 (2023) 12132–12139.
[62] Y. Wu, N. Joshi, S. Zhao, H. Long, L. Zhou, G. Ma, B. Peng, O.N. Oliveira Jr, A. Zettl, L. Lin, NO2 gas sensors based on CVD tungsten diselenide monolayer, Appl. Surf. Sci. 529 (2020) 147110.
[63] Z. Xiao, Y. Hu, J. Hu, H. Wang, J. Ji, J. Huang, C. Xing, Coordination environment tuning of Ni-Sn catalysts by glu-carbon to optimize cellulose hydrogenolysis to oxygenated chemicals, Fuel 350 (2023) 128833.
[64] X. An, Y. Li, S. Ni, Z. Wang, M. Song, Grain refinement process in a cold-rolled polycrystalline cobalt, Mater. Charact. 164 (2020) 110360.
[65] X.-L. Shi, W.D. Liu, A.-Y. Wu, V.T. Nguyen, H. Gao, Q. Sun, R. Moshwan, J. Zou, Z.-G. Chen, Optimization of sodium hydroxide for securing high thermoelectric performance in polycrystalline Sn1 − xSe via anisotropy and vacancy synergy, InfoMat 2 (2020) 1201–1215.
[66] S. Ning, J. Wang, D. Xiang, S. Huang, W. Chen, S. Chen, X. Kang, Electrochemical reduction of SnO2 to Sn from the Bottom: In-Situ formation of SnO2/Sn heterostructure for highly efficient electrochemical reduction of carbon dioxide to formate, J. Catal. 399 (2021) 67–74.
[67] P.V. Tuan, H.B. Tuong, V.T. Tan, L.H. Thu, N.D. Khoang, T.N. Khiem, SnO2/reduced graphene oxide nanocomposites for highly efficient photocatalytic degradation of methylene blue, Opt. Mater. 123 (2022) 111916.

[68] M. Vandana, S. Veeresh, H. Ganesh, Y.S. Nagaraju, H. Vijeth, M. Basappa, H. Devendrappa, Graphene oxide decorated SnO2 quantum dots/polypyrrole ternary composites towards symmetric supercapacitor application, J. Energy Storage 46 (2022) 103904.
[69] S. Bai, Y. Xu, K. Cao, X. Huang, Selective ethanol oxidation reaction at the Rh–SnO2 interface, Adv. Mater. 33 (2021) 2005767.
[70] M.G. Chae, S.H. Han, B.K. Park, T.-M. Chung, J.H. Han, Atomic-layer-deposited SnO film using novel Sn(dmamb)2 precursor for p-channel thin film transistor, Appl. Surf. Sci. 547 (2021) 148758.
[71] Y. Hu, C. Yue, J. Wang, Y. Zhang, W. Fang, J. Dang, Y. Wu, H. Zhao, Z. Li, Fe–Ni metal–organic frameworks with prominent peroxidase-like activity for the colorimetric detection of Sn2+ ions, Analyst 145 (2020) 6349–6356.
[72] L. Liu, Y. Wang, K. Guan, Y. Liu, Y. Li, F. Sun, X. Wang, C. Zhang, S. Feng, T. Zhang, Influence of oxygen vacancies on the performance of SnO2 gas sensing by near-ambient pressure XPS studies, Sens. Actuators B Chem. 393 (2023) 134252.
[73] A. Ahmed, M.N. Siddique, T. Ali, P. Tripathi, Defect assisted improved room temperature ferromagnetism in Ce doped SnO2 nanoparticles, Appl. Surf. Sci. 483 (2019) 463–471.
[74] F. Li, S. Ruan, N. Zhang, Y. Yin, S. Guo, Y. Chen, H. Zhang, C. Li, Synthesis and characterization of Cr-doped WO3 nanofibers for conductometric sensors with high xylene sensitivity, Sens. Actuators B Chem. 265 (2018) 355–364.
[75] A. Mirzaei, K. Janghorban, B. Hashemi, M. Bonyani, S.G. Leonardi, G. Neri, A novel gas sensor based on Ag/Fe2O3 core-shell nanocomposites, Ceram. Int. 42 (2016) 18974–18982.
[76] Shrisha, C.-M. Wu, K.G. Motora, G.-Y. Chen, D.-H. Kuo, N.S. Gultom, Highly efficient reduced tungsten oxide-based hydrogen gas sensor at room temperature, Mater. Sci. Eng. B 289 (2023) 116285.
[77] W. Yan, C. Lv, D. Zhang, Y. Chen, L. Zhang, C.Ó. Coileáin, Z. Wang, Z. Jiang, K.-M. Hung, C.-R. Chang, H.-C. Wu, Enhanced NO2 sensitivity in schottky-contacted n-type SnS2 gas sensors, ACS Appl. Mater. Interfaces 12 (2020) 26746–26754.
[78] T.P. Mokoena, H.C. Swart, D.E. Motaung, A review on recent progress of p-type nickel oxide based gas sensors: future perspectives, J. Alloy. Compd. 805 (2019) 267–294.
[79] N. Wang, W. Tao, X. Gong, L. Zhao, T. Wang, L. Zhao, F. Liu, X. Liu, P. Sun, G. Lu, Highly sensitive and selective NO2 gas sensor fabricated from Cu2O-CuO microflowers, Sens. Actuators B Chem. 362 (2022) 131803.
[80] E.H. Kwon, H. An, M.B. Park, M. Kim, Y.D, Park Conjugated polymer–zeolite hybrids for robust gas sensors: Effect of zeolite surface area on NO2 sensing ability, Chem. Eng. J. 420 (2021) 129588.
[81] A.A. Mane, M.P. Suryawanshi, J.H. Kim, A.V. Moholkar, Highly slelective and sensitive response of 30.5% of sprayed molybdenum trioxide (MoO3) nanobelts for nitrogen dioxide (NO2) gas detection, J. Colloid Interf. Sci. 483 (2016) 220–231.
[82] J.J. Qi, S. Gao, K. Chen, J. Yang, H. Wh. Zhao, L. Guo, S.H. Yang, Vertically aligned, double-sided, and self-supported 3D WO3 nanocolumn bundles for low temperature gas sensing, J. Mater. Chem. A 3 (2015) 18019–18026.
[83] J. Shi, Z. Cheng, L. Gao, Y. Zhang, J. Xu, H. Zhao, Facile synthesis of reduced graphene oxide/hexagonal WO3 nanosheets composites with enhanced H2S sensing properties, Sens. Actuators B Chem. 230 (2016) 736–745.
[84] S. Harbeck, A. Szatvanyi, N. Barsan, U. Weimar, V. Hoffmann, DRIFT studies of thick film un-doped and Pd-doped SnO2 sensors: temperature changes effect and CO detection mechanism in the presence of water vapour, Thin Solid Films 436 (2003) 76–83.
[85] N. Yamazoe, K. Suematsu, K. Shimanoe, Two types of moisture effects on the receptor function of neat tin oxide gas sensor to oxygen, Sens. Actuators B Chem. 176 (2013) 443–452.
[86] Y. Xiong, Y. Lin, X. Wang, Y. Zhao, J. Tian, Defect engineering on SnO2 nanomaterials for enhanced gas sensing performances, Adv. Powder Mater. 1 (2022) 100033.
[87] I. Barin, Therrnochernical data of pure substances (VCH Verlagsgesellschaft mbH. D-69451 Weinheim, 1995).

Changhyun Jin received his Ph.D. degree in Materials Science and Engineering from Inha University, South Korea, in 2013. He is currently a research professor at the Department of Materials Science and Engineering, Yonsei University. His areas of interest are (i) synthesis of inorganic nanostructures with controlled dimension, (ii) interaction between inorganic nanostructures and chemicals, and (iii) optical properties of nanostructure arrays and aggregates.

Hyunseong Yang received a Bachelor's degree in Bio medical Engineering at Yonsei University in 2022. Since 2022, he is currently studying on semiconductor gas sensors as a Master's student under the guidance of Prof. Wooyoung Lee at Yonsei University.

Taewon Lim received a Bachelor's degree in Material Science and Engineering at Kyungsung University in 2023. Since 2023, he is currently studying on semiconductor gas sensors as a Master's student under the guidance of Prof. Wooyoung Lee at Yonsei University.

Kyu Hyong Lee is currently a professor in the Department of Materials Science and Engineering at Yonsei University in Seoul, Korea. He received his Ph.D. in ceramic engineering from Yonsei University in 2005. From 2005–2007, he worked as a postdoctoral research fellow at Nagoya University. Since 2007, he has been a research staff member and since 2010 project leader at the Samsung Advanced Institute of Technology. His research activity has focused on the development of high-performance thermoelectric materials and functional oxides.

Wooyoung Lee is the Underwood distinguished professor of the Department of Materials Science and Engineering at Yonsei University in Korea. He is also the Director of the Center for Super Critical Material Industrial Technology, National Core Materials Research Center and the institute of Korea Initiative for Fostering University of Research and Innovation. He is the President of The Korean Magnetics Society and a regular member of the National Academy of Engineering of Korea. In recent years, his research interests have centered on hydrogen sensors, various metal oxide semiconducting gas sensors, and breath analyzers. He is also studying rare-earth permanent magnets and thermoelectric materials and devices. He has received a number of awards in nano-related research areas including a Prime Minister Award (2023) in Nano Korea 2023, SeAH-Haiam Fellowship Award (2018) in The Korean Institute of Metals and Materials and a Service Merit Medal (2008) from the Government of Korea due to his contribution to the development of intellectual properties. He has authored and co-authored over 280 publications and has edited three special books on nanostructured materials and devices.